RESEARCH ARTICLE
PLANETARY SCIENCES

Earth and Planetary Physics
7: 161–192, 2023
doi: 10.26464/epp2023031

Formation and modification of wrinkle ridges in the central Tharsis region of Mars as constrained by detailed geomorphological mapping and landsystem analysis

An Yin*, and YingChi Wang

Department of Earth, Planetary, and Space Sciences, University of California, Los Angeles, CA 90095-1567, USA

Key Points:

- Wrinkle ridges in the Tharsis region of Mars were induced by decollement folding.
- Folding occurred during flood-basalt volcanism.
- Undeformed basement of the folded strata was subducted below the volcanic eruption zone.
- Regional glaciation across the Tharsis rise modified the original shapes of the wrinkle ridges.

Citation: Yin, A., and Wang, Y. C. (2023). Formation and modification of wrinkle ridges in the central Tharsis region of Mars as constrained by detailed geomorphological mapping and landsystem analysis. *Earth Planet. Phys.*, *7*(2), 161–192. http://doi.org/10.26464/epp2023031

Abstract: Wrinkle ridges are common landforms documented on all rocky planets and the Moon in the inner solar system. Despite the long research history, their formation mechanisms remain debated. A key unresolved issue is whether the wrinkle-ridge formation is related to igneous processes. This is because wrinkle ridges are mostly associated in space and possibly in time with the occurrence of flood-basalt volcanism in all cases in the inner solar system. To address this issue, we conducted geomorphological mapping, a topographic-data analysis, and a detailed landform and landsystem analysis of satellite images at a resolution of 25 cm/pixel to 6 m/pixel in the central Tharsis region of Mars. The main results of this work are in the form of (1) a regional geomorphological map at a resolution of 6 m/pixel and (2) a local geomorphological map at a resolution of 50 cm/pixel. Our work suggests the following older-to-younger sequence of geological events in the study area: (1) formation of a northeast-trending mountain range (i.e., the Thaumasia plateau) along the eastern margin of the Tharsis rise that was created by the Himalayan-style crustal-scale thrusting; (2) coeval volcanic-plateau construction west of the thrusting-induced rising mountain range; (3) eastward-flowing lavas that were sourced from a volcanic plateau to the west terminated at the rising Thaumasia plateau to the east; (4) wrinkle-ridge development by decollement folding of recently emplaced warm, ductile volcanic-lava piles; (5) emplacement of a regionally extensive ice sheet over the central Tharsis region that produced extensive boulder-bearing materials, striated surfaces, and boulder-bearing dendritic-ridge networks possibly representing subglacial eskers; and (6) local deposition of highly concentrated glacial flours resulted in the formation of mantled terrain on plains between wrinkle ridges. Our work supports the early suggestion that the Tharsis wrinkle ridges were created by horizontal shortening induced by crustal-scale tectonic processes. In detail, however, the occurrence of flow-front-like fold margins associated with many mapped wrinkle ridges suggests the involvement of ductile-flow deformation during ridge formation. We attribute the flow-like fold fronts to ductile deformation of thermally weakened lava piles that were emplaced during or immediately before the folding event. Our compression-induced wrinkle-ridge model also differs from the early hypotheses in that the thin-skinned folding is associated with basement subduction, which explains the lack of coeval and parallel folding and extensional faulting associated with wrinkle ridge formation in the study area. Post-folding glacial modification means that the present wrinkle-ridge morphologies may differ significantly from the original fold shapes, which prevents the utility of using topographic profiles across wrinkle ridges for inverting the underlying thrust geometries.

Keywords: planetary tectonics; wrinkle ridges; Tharsis rise; glaciation

1. Introduction

Wrinkle ridges are linear or sinuous arch-shaped topographic features that are commonly superposed by smaller sharp-crested crenulated ridges (e.g., Watters, 1988; Andrews-Hanna, 2020). Wrinkle ridges, originally referred to by Elger (p. 12, 1895) as "mountain ridges" on flat mare plains of the Moon, were assigned by Fielder (1965) and Guest and Fielder (1968) as a subclass of "elementary rings". These features are later classified as a distinctive class of landforms on the Moon referred to as "wrinkle ridges" (Fielder, 1961, 1965; Fielder and Kiang, 1962). Subsequent work on lunar wrinkle ridges has quantified their map-view patterns, cross-sectional shapes, spatial distributions, geologic contexts, and formation ages (e.g., Tjia, 1970; Strom, 1972; Bryan, 1973; Plescia

Correspondence to: A. Yin, ayin54@gmail.com
Received 11 DEC 2022; Accepted 13 FEB 2023.
Accepted article online 28 FEB 2023.

and Golombek, 1986; Watters, 1988, 2022; Yue Z et al., 2015, 2017; Li B et al., 2018). Images collected by spacecrafts through the inner solar system show that linear and sinuous positive landforms similar to lunar wrinkle ridges occur on all rocky planets (Golombek et al., 1991): (1) Mercury (Murray et al., 1974; Strom et al., 1975; Strom, 1979; Maxwell and Gifford, 1980; Murchie et al., 2008; Watters et al., 2009a, b; Byrne et al., 2014; Crane and Klimczak, 2019; Schleicher et al., 2019; Watters, 2021), (2) Venus (Watters, 1992; McGill, 1993, 2004; Kreslavsky and Basilevsky, 1998; Bilotti and Suppe, 1999; Basilevsky and Head, 2006; Hansen and Olive, 2010; Ivanov and Head, 2011; Byrne et al., 2021; Bethell et al., 2022), (3) Mars (Wilhelms, 1974; Carr et al., 1977; Greeley and Spudis, 1978a, b; Lucchitta, 1978; Lucchitta and Klockenbrink, 1981; Watters, 1991, 1993; Zuber 1995; Watters and Robinson, 1997; Mangold et al., 1998; Schultz, 2000; Golombek et al., 2001; Head et al., 2002; Montési and Zuber, 2003; Mueller and Golombek, 2004; Ruj and Kawai, 2021; Karagoz et al., 2022a, b), and (4) the Earth (Reidel, 1984; Plescia and Golombek, 1986). A shared characteristic of wrinkle ridges on the rocky planets and the Moon is that their formation is closely associated in space and possibly in time with flood-basalt volcanism (e.g., Plescia and Golombek, 1986; Watters, 1988).

Wrinkle-ridge formation has been attributed to horizontal shortening, and the required compressive stresses are thought to have originated from (1) flexural bending of the lithosphere caused by lava-fill-induced loading (e.g., Baldwin, 1968; Maxwell et al., 1975) or (2) the sinking of high-density bodies in the viscous mantle that caused downward warping of the crust (Phillips et al., 1972; Solomon and Head, 1979, 1980; Freed et al., 2001). Tjia (1970) noted that some lunar wrinkle ridges display *en echelon* patterns in map view, which imply their formation by strike-slip shear deformation with basement-involved faulting cutting deep into the lunar crust. Tjia's (1970) hypothesis assumes the ridges to represent compression-induced folds. While agreeing that the wrinkle ridges likely represent folds, Rahn (1971) questioned Tjia's (1970) strike-slip interpretation. Instead, Rahn (1971) suggested that the lunar wrinkle ridges may have been induced by topographically induced gravitational sliding. The model envisioned by Rahn (1971), schematically shown in Figure 1a with an implied thin-skinned origin of the fold-generated ridges, is similar to the later model of Cassanelli and Head (2019), who proposed the formation of wrinkle ridges in the central Tharsis region of Mars above a regional ice-bearing décollement. Cassanelli and Head's (2019) model requires a sequential emplacement of lava beds during decollement folding (see the evolutionary stage 1 to stage 3 in Figure 1b).

An alternative view of the wrinkle-ridge formation appeals for igneous processes (e.g., Fielder, 1961). Strom (1972) best articulated this hypothesis by showing that some lunar wrinkle ridges exhibit lava-flow-like landforms that can be interpreted as shallow-extrusive igneous bodies. Strom (1972) envisioned that the wrinkle-ridge arches were created by the emplacement of elongated laccolith bodies (Figure 1c), which were sourced from deep-seated, preexisting, crustal-scale fractures formed by earlier impacting and tectonic deformation. Strom (1972) further suggested that the secondary crenulated ridges on top of the wrinkle-ridge arches are extrusive volcanic landforms emerging from tensile fractures along ridge crests (also see Guest, 1971).

Bryan (1973) showed, based on detailed mapping and satellite-image analysis, that his mapped lunar wrinkle ridges consistently cut across lava-flow-like landforms. This observation rules out the laccolith-dome model of Strom (1972) in his mapping area as the general cause of wrinkle-ridge formation. Mapping by Howard and Muehlberger (1973) reached the same conclusion. The close association of their mapped lunar wrinkle ridges with ridge-bounding scarps led Howard and Muehlberger (1973) to interpret the ridges and ridge-bounding scarps as folds and thrusts, respectively, above a décollement. The hypothesis of Howard and Muehlberger (1973), schematically shown in Figure 1d, is perhaps the first that explicitly invoked the thin-skinned deformation as the cause of wrinkle-ridge formations in the solar system. Similar décollement-fold models for wrinkle-ridge formation on Mars were also proposed (Watters, 1988, 1991). In Watters (1988), décollement folding is considered to have occurred either during or after lava emplacement (Figure 1f). Watters (1991) envisioned that the Martian fold décollement zone follows a lava-covered regolith layer, which is weaker than the basement rocks below and the lava flows above (see the sketch in Figure 1e based on the model envisioned by Watters, 1991; see also Mangold et al., 1998).

In contrast to the décollement model mentioned above, Zuber and Aist (1990) and Allemand and Thomas (1995) argued that wrinkle-ridge formation on Mars can be explained by crustal-scale thrusting (i.e., thick-skinned deformation) and that the fold-generating thrust systems may also involve secondary back thrusts (Figure 1g). Plescia and Golombek (1986) proposed that deep-skinned wrinkle ridges on the Moon, Mercury, and Mars may represent thrust-related fault-bend or fault-propagation folds observed widely on Earth (Figure 1h). A key prediction of the thick-skinned model is that the blind thrusts below the wrinkle ridges extend downward to and merge into the ~30-km-deep, flat décollement zone at the brittle-ductile transition depth (e.g., Allemand and Thomas, 1995). As predicted by the classic fault-bend fold model (Suppe, 1983), motion along 30-km-deep thrust ramps dipping at 30° would have produced uplifts with their horizontal dimensions equivalent to the horizontal length of the ramps, which is on the order of ~52 km. A variation of the thick-skinned thrusting model is the addition of back thrusts above the main thrusts, which were thought by Okubo and Schultz (2004) to have been closely related to the formation of wrinkle ridges. In the model proposed by Okubo and Schultz (2004), motion on the primary thrust generates the broad arch represented by the wrinkle ridge above; meanwhile, secondary branching thrusts create smaller crenulated ridges (Figure 1i). The mechanical plausibility of basement-involved thrusting for wrinkle-ridge formation was further demonstrated by Montési and Zuber (2003); their work showed that wrinkle ridges were likely developed as folds involving the 20- to 40-km-thick upper crust.

Note that the thin-skinned model requires the presence of an undeformed footwall below the flat décollement that bounds the folds above. To our knowledge, exactly how the footwall is shortened during the proposed thin-skinned folding has never been discussed in the literature. Although the thick-skinned thrusting

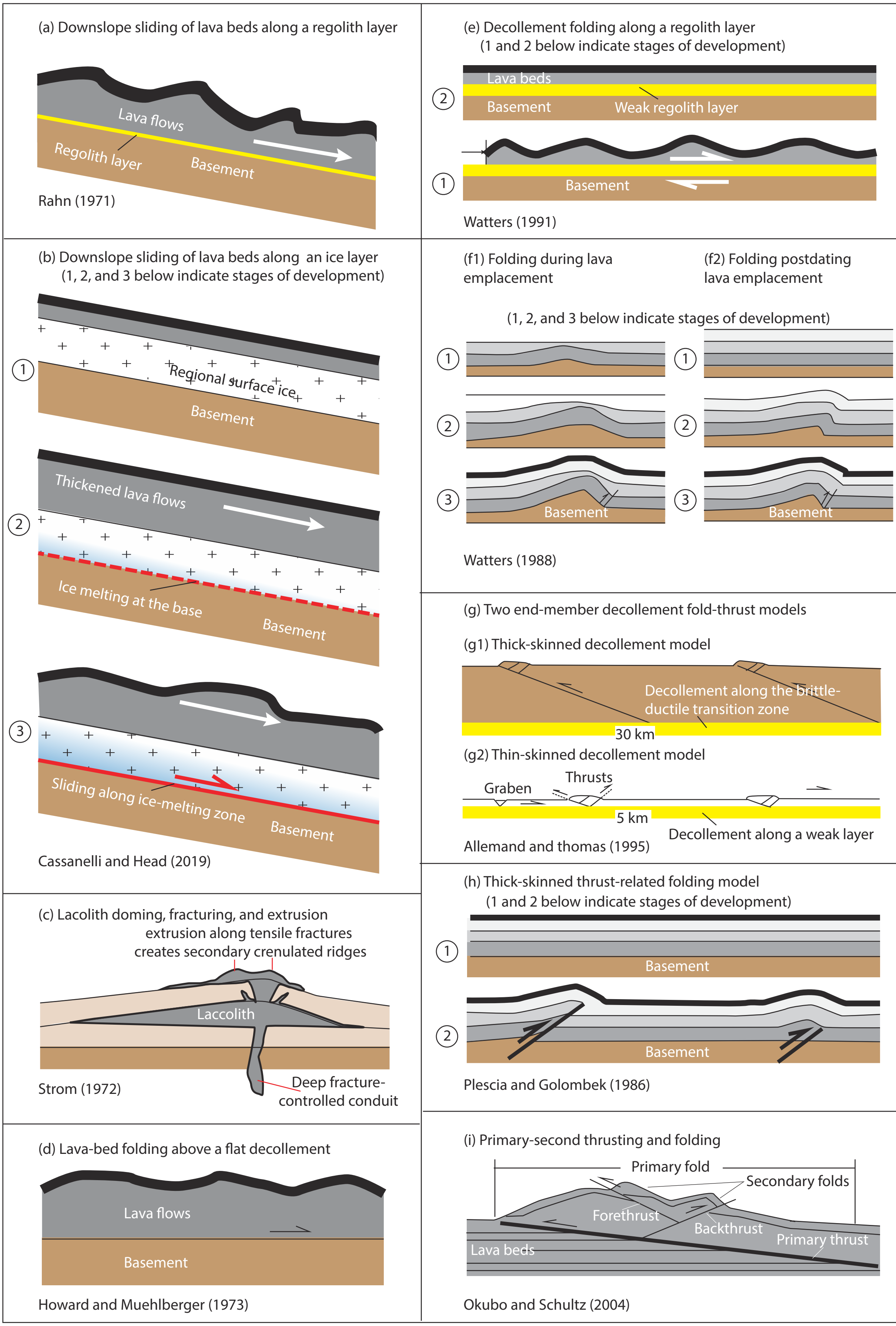

Figure 1. (a–i) Competing models for wrinkle-ridge formation. See text for details.

model places the décollement at a greater depth (Allemand and Thomas, 1995; Mueller and Golombek, 2004), this class of model faces the same issue and does not explain how the shortening below the deep-seated décollement is absorbed during wrinkle-ridge formation. Observations supporting the thin-skinned model (i.e., that décollements are within the brittle upper crust) include short dimensions (i.e., only a few kilometers wide) of wrinkle ridges (Karagoz et al., 2022b), whereas observations supporting the thick-skinned models come from unidirectionally dipping thrusts that bound parallel wrinkle ridges on sloping terrain on Mars (Golombek et al., 2001). More recently, Andrews-Hanna (2020) used a Monte Carlo boundary-element model to show that the topographic profiles of wrinkle ridges, if they still represent the original fold shapes, can be explained by a range of subsurface thrust configurations involving thin- and thick-skinned styles of deformation.

The literature review above raises two issues. First, the models for the formation of wrinkle ridges are all based on local geological observations. Because of this, it is possible that wrinkle ridges could have been created by multiple location-specific mechanisms, leading to similar ridge shapes. Second, in all the quantitative models for wrinkle-ridge formation, topographic profiles are regarded as representing the original fold shapes that can be used for inverting the geometry, slip magnitude, and décollement depth of the inferred subsurface thrusts (e.g., Schultz, 2000; Mueller and Golombek, 2004; Watters, 2004; Andrews-Hanna, 2020; Watters, 2021; Karagoz et al., 2022b; cf. Mège and Reidel, 2001). We noted that in the Tharsis region of Mars, where this study was conducted, protracted volcanism since ~3.8 Ga has been documented (e.g., Carr, 1973; Neukum et al., 2004; Baptista et al., 2008; Hauber et al., 2009; Richardson et al., 2013, 2021; Mouginis-Mark et al., 2022). Additionally, open-water fluvial processes (Mangold et al., 2008; Ansan and Mangold, 2006, 2013), glacial deposition and erosion (e.g., Fueten et al., 2011; Mège and Bourgeois, 2011; Brunetti et al., 2014; Gourronc et al., 2014; Dębniak et al., 2017; Grau Galofre et al., 2020; Yin A et al., 2021; Kakaria and Yin A, 2023), and eolian processes (Ward et al., 1985; Edgett, 1997; Bridges et al., 2010; Berman et al., 2011) have all been documented. Hence, whether geological processes postdating wrinkle-ridge formation have significantly modified the original ridge morphologies requires a detailed, systematic assessment, which is the focus of this study.

2. Regional Setting of the Study Area

The study area is located in the Solis Dorsa wrinkle-ridge field of the central Tharsis rise (Figure 2). The area is bounded by Sinai Planum, Valles Marineris, Thaumasia Planum, and Solis Planum, respectively (Figure 2). The Tharsis rise is the youngest, topographically highest volcanic-tectonic province on Mars and hosts the tallest shield volcanoes on the planet (Smith et al., 1999; Solomon et al., 2005; Tanaka et al., 2014). The interpreted tectonic history of the Tharsis rise has been focused on (1) whether its topography was created rapidly in the Late Noachian at ~3.8 Ga (Phillips et al., 2001; Carr and Head, 2010; Cassanelli and Head, 2019) or slowly and continuously from ~3.8 Ga to the present (Zuber, 2001; Neukum et al., 2004; Solomon et al., 2005; Nimmo and Tanaka, 2005; Zhong SJ, 2009; Golombek and Phillips, 2010; Yin A, 2012a; Tanaka et al., 2014) and (2) the relative importance of tectonic processes, igneous processes, and some forms of their combination in creating the Tharsis rise (Solomon and Head, 1982; Neukum et al., 2004; Hauber et al., 2009; Zhong SJ, 2009; Mangold et al., 2010; Yin A, 2012a, b; Richardson et al., 2013, 2021; Tanaka et al., 2014; Bouley et al., 2018; Cassanelli and Head, 2019; Mouginis-Mark and Wilson, 2019). The igneous-process models for Tharsis formation advocate the role of mantle upwelling and the resulting partial melting in contributing to magmatic underplating and crustal thickening of the Tharsis region (Carr, 1974; Wise et al., 1979; Harder and Christensen, 1996; Mège and Masson, 1996a, b; Baker et al., 2007; Dohm et al., 2007; Zhong SJ, 2009). Alternatively, juvenile-crust formation through diking (Lillis et al., 2009) or thick (5–10 km) volcanic deposition from the top (Solomon and Head, 1982) have been proposed as crustal thickening and uplift mechanisms for the Tharsis development. Mantle melting induced by giant impacts as the cause of magmatic underplating or volcanic eruptions has also been suggested (Solomon and Head, 1982; Reese et al., 2004; Golabek et al., 2011). The volcanic-loading models, such as that proposed by Solomon and Head (1982), predict surficial compressional deformation around the center of the load and extension across the rim zone of the load. In contrast, the magmatic underplating model predicts upward doming leading to extension in the center of the subsurface load and radial compression across the rim zone of the underplating center (e.g., Tanaka et al., 1991; Banerdt et al., 1992).

Tectonic processes may also have been responsible for the formation of the Tharsis rise and the early Mars topography (Stevenson, 2001). For example, Sleep (1994) proposed that the western half of the Tharsis rise consisting of the Tharsis Montes, Olympus Mons, and Alba Mons was constructed by subduction-induced arc development. Expanding on this idea, Yin A (2012a) constructed a primitive plate-tectonic model that predicts the entire Tharsis rise to have been formed by subduction-induced extension expressed as diking during slab rollback. This model requires local thermal-boundary-layer recycling (Yin A, 2012a), the horizontal translation of rigid blocks (Yin A, 2012b; Dohm et al., 2018), and compressional tectonics across the eastern Tharsis rise as a result of retro-arc shortening (Yin A, 2012a). The primitive plate-tectonic model of Yin A (2012a, b) differs from the modern plate tectonics on Earth in that the latter hosts plate-tectonic processes at a global scale. The formation of the Tharsis rise has also been related to mantle upwelling induced by convective removal of the Tharsis mantle lithosphere (Scott and Wilson, 2003). Additionally, the development of a stationary hot spot (Carr, 1974) or a migrating mantle-upwelling sheet (Zhong SJ, 2009) may have caused the formation of the Tharsis rise.

Examining Viking images led to the recognition of wrinkle ridges on Mars (Wilhelms, 1974; Carr et al., 1977; Greeley and Spudis, 1978a, b; Lucchitta, 1978). Detailed mapping allowed Lucchitta and Klockenbrink (1981) to classify Martian wrinkle ridges into two types: Type-1 ridges, which have linear traces and occur exclusively in smooth-plain terrain, and Type-2 ridges, which have curvilinear traces with an anastomosing pattern that occur exclusively in cratered terrain. Lucchitta and Klockenbrink (1981)

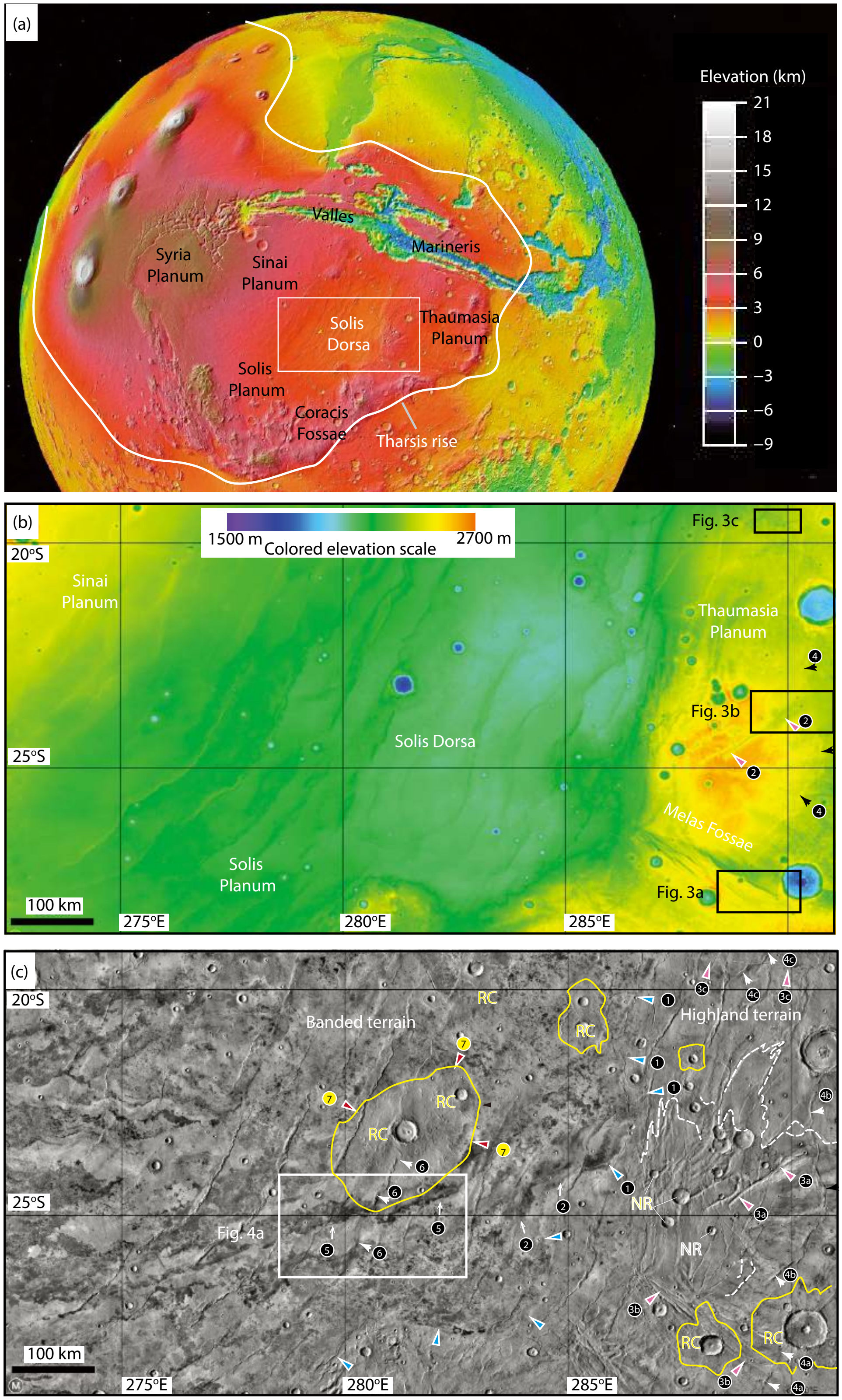

Figure 2. (a) A Google Mars image of the Tharsis rise of Mars. The image also shows the geographic locations of Sinai Planum, Valles Marineris, Thaumasia Planum, Coracis Fossae, Solis Planum, and Syria Planum. (b) A digital elevation model (DEM) map of Solis Dorsa and its surrounding areas. Also shown in this image are the locations of Figures 3a–3c. (c) A black-and-white map of nighttime temperatures that is blended with a THEMIS image, a CTX image, and a shaded DEM relief map. Darker toned areas indicate higher nighttime temperatures. The numbers are geologic features described in the text, and yellow lines outline the extent of viscous-flow ejecta deposits of rampart-type impact craters, marked as RC. Craters without a well-defined impact ejecta apron and rim ridges occur in the highest elevation area of Thaumasia Planum and are marked as NR for non-rampart-type impact craters. The white box marks the location of Figure 4a.

attributed the formation of Type-1 ridges to horizontal shortening and Type-2 ridges to differential uplifts during high-angle faulting.

Plescia and Golombek (1986) also concluded that Martian wrinkle ridges had been created by tectonic shortening and considered them expressions of thick-skinned, thrust-related fault-bend and fault-propagation folds (Figure 1g; see also Mueller and Golombek, 2004). Their interpretation is supported by the similar morphology of Martian wrinkle ridges with a suite of thrust-related folds on Earth. Several researchers have shown that scarps bounding wrinkle ridges appear to offset crater rims and crater floors at a few localities in the Tharsis region (Allemand and Thomas, 1995; Karagoz et al., 2022a, b). Cole and Andrews-Hanna (2017) interpreted a ridge-forming landform cutting obliquely across beddings exposed on a steep trough wall of Valles Marineris as a thrust zone, because it could be projected below a nearby wrinkle ridge.

Lava emplacement from fissure volcanic constructs has also been documented in the plateau region of the central Tharsis rise (Hauber et al., 2009; Richardson et al., 2013, 2021). Volcanic-plain construction in the plateau region was accommodated by the emplacement of flat-topped lobate ridges that are tens to more than hundreds of kilometers in length (Carr, 1973; Carr et al., 1977; De Hon, 1982; Dohm and Tanaka, 1999; Zhao J et al., 2017) trending parallel to the regional slope (Mouginis-Mark et al., 1982; Zhao J et al., 2017). The lava plains are superposed by isolated, sinuous ridges with lengths varying between ~14 and ~740 km (Zhao J et al., 2017). The age of the isolated ridges is dated to be dominantly Late Hesperian, whereas the ridge formation has been related to lava emplacement (Zhao J et al., 2017).

Wrinkle ridges are best developed across the Tharsis rise and its neighboring regions (Tanaka et al., 2014; Ruj and Kawai, 2021). The ridges trend parallel in the north to northeast direction regardless of their locations across the Tharsis rise. Driving mechanisms for the formation of wrinkle ridges on Mars have been debated, with the current models invoking volcanic loading (Phillips and Lambeck, 1980), planetary cooling (Schubert et al., 1992; Nahm and Schultz, 2011; Andrews-Hanna, 2020), and subduction-induced compression (Yin A, 2012a). Note that the volcanic-loading and global-cooling models predict spatially varying compressional directions while the subduction model predicts unidirectional compression across the Tharsis rise and its marginal zone. Globally, crater dating shows that wrinkle ridges on Mars were formed mostly in the Early Hesperian (3.66–3.40 Ga; Ruj and Kawai, 2021), coeval during the planet-wide volcanic emplacement (Tanaka et al., 2014). However, younger and locally developed wrinkle ridges with Late Hesperian (~3.14 Ga) and Amazonian ages (~2.52 Ga) are also present (Ruj and Kawai, 2021).

3. Data and Methods

Regional topographic maps were constructed by blending High-Resolution Stereo Camera (HRSC) data collected by the Mars Express orbiter with Mars Orbiter Laser Altimeter (MOLA) data (200 m/pixel) collected by the Mars Global Surveyor orbiter (Fergason et al., 2018; Figure 2). The blended Digital Elevation Model (DEM) was superposed over a global mosaic of Thermal Emission Imaging System (THEMIS) daytime-infrared images at a resolution of 100 m/pixel (Edwards et al., 2011; Fergason et al., 2018) or a global mosaic of Context Camera (CTX) images (Dickson et al., 2018) at a resolution of ~6 m/pixel obtained by the Mars Reconnaissance Orbiter (Malin et al., 2007). We performed the aforementioned data superposition by using the Java Mission-planning and Analysis for Remote Sensing (JMARS) GIS software package of Christensen et al. (2009). Our geomorphological mapping was conducted by using High-Resolution Imaging Science Experiment (HiRISE) images at a resolution of 25 cm/pixel. The HiRISE images were displayed and analyzed using the HiView software available at https://www.uahirise.org/hiview/. The final geomorphological map was drafted by using Adobe Illustrator.

Interpreting the formation processes of a mapped landform can be highly nonunique. To enhance the likelihood of the interpreted formation mechanism for an observed landform assemblage, in this study we adopted a landsystem approach (e.g., Evans, 2003; Yin A et al., 2021; Chen HZ and Yin A, 2022). Specifically, we sought a landsystem model capable of explaining (1) the relationship between the morphology and sedimentology of individual landforms and (2) the formation of all spatially and temporally related landforms in the assemblage. The landsystem approach has been proven successful for geomorphological research on Mars in the work of Head et al. (2010); Gallagher and Balme (2015); Butcher et al. (2016, 2017), and Dębniak et al. (2017), to name a few.

4. Results

4.1 Geological Context of the Solis Dorsa Wrinkle-Ridge Field

Solis Dorsa is a northeast-trending oval-shaped basin that is ~800 km wide in the northwest–southeast direction and 1,200 km long in the northeast–southwest direction (Figure 2). The first-order cross-cutting relationships among the major topographic features could be deciphered by using the DEM map and the nighttime temperature map of the region (Figures 2b and 2c). The oldest terrain is the eastern highland region of Thaumasia Planum (also known as the Thaumasia plateau or Thaumasia highlands); its western boundary (*feature 1* in Figure 2c) truncates east-northeast-trending darker and lighter toned bands in the Solis Dorsa region (*feature 2* in Figure 2c), which are together referred to as the “banded terrain” in this study. The highland terrain itself is cut by linear grooves that trend northeast (*feature 3a* in Figure 2c), northwest (*feature 3b* in Figure 2c), and east (*feature 3c* in Figure 2c), respectively. The grooves are in turn superposed by north-trending wrinkle ridges in the highland terrain (*features 4a, 4b,* and *4c* in Figure 2c). East-northeast-trending darker toned stripes (*feature 5* in Figure 2c) in the banded terrain are also superposed by the north- and northeast-trending wrinkle ridges (*feature 6* in Figure 2c).

Two types of craters occur in the study area: (1) rampart craters characterized by layered viscous-flow-like ejecta-blanket deposits (*feature RC* and yellow lines that outline the extent of the impact deposits in Figure 2c), and (2) non-rampart-like craters characterized by simple rim ridges and circular ejecta-blanket deposits

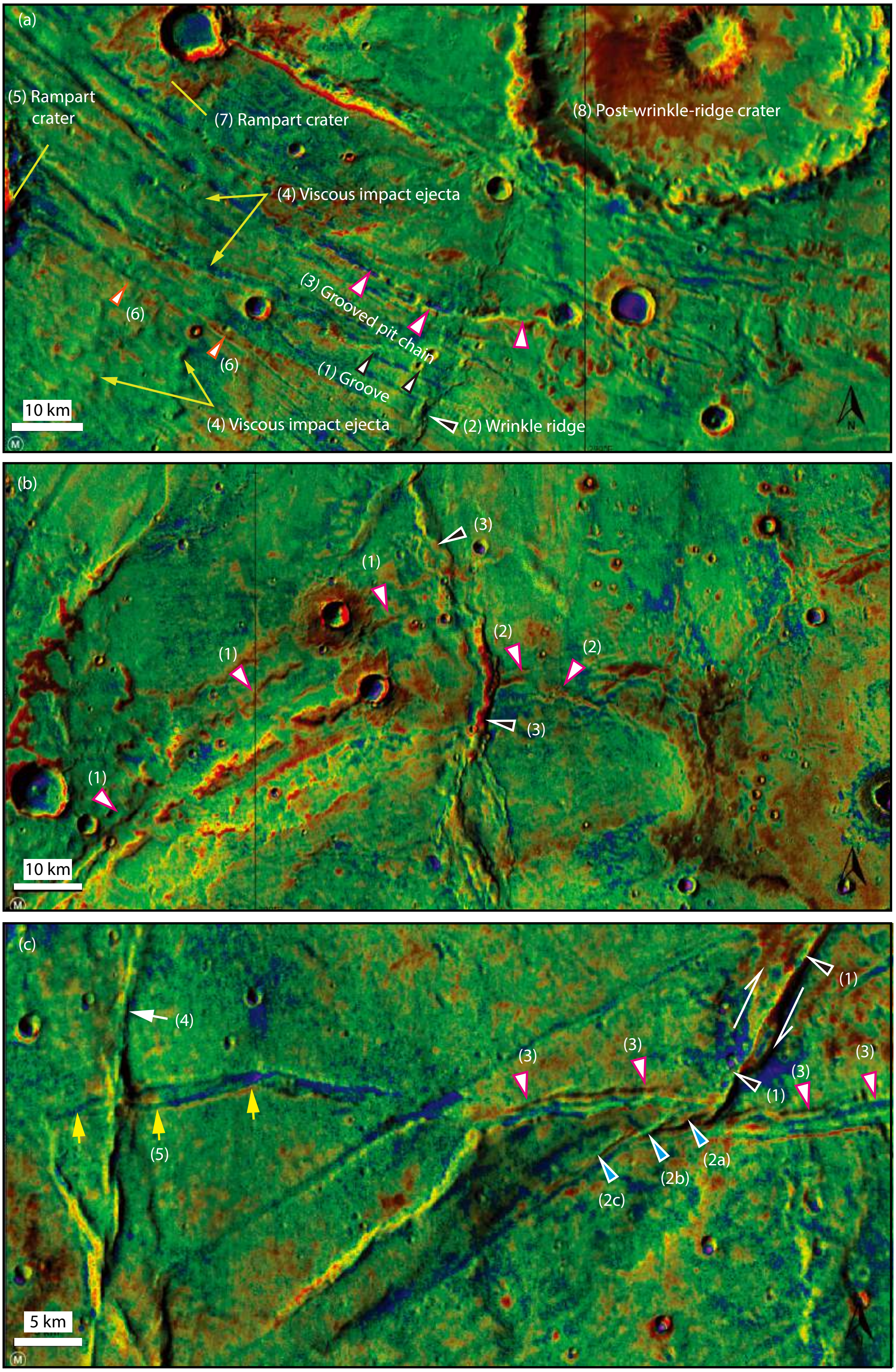

Figure 3. (a–c) Colored nighttime temperature maps that are blended with a THEMIS image, a CTX image, and a shaded digital elevation model relief map. Brighter colored areas indicate higher nighttime temperatures. The numbers refer to landform features described in the text. See Figure 2 for the locations of the three panels.

(*feature NR* in Figure 2c). The largest rampart crater ejecta-blanket deposits (*feature 7* in Figure 2c) in the banded terrain are superposed over the nearby wrinkle ridges (*feature 6* in Figure 2c). We noted that rampart craters occur throughout the banded terrain. However, this is not the case for the highland terrain, in which craters in the highest topographic region are nonrampart types: they show well-defined central uplifts and rim ridges, but they lack viscous-flow-like ejecta-blanket deposits. Sinuous, finger-shaped scarps are present in the highland terrain, but no obvious craters can be correlated with these features (white dashed lines in Figure 2c).

The detailed relationship between grooves in the highland terrain and wrinkle ridges is further illustrated in the zoomed-in image in Figure 3. Here, a northwest-trending linear groove (*feature 1* in Figure 3a) is terminated and superposed by a northeast-trending wrinkle ridge (*feature 2* in Figure 3a). Also shown in Figure 3a is a curvilinear, grooved pit chain (*feature 3*) that cuts across the same wrinkle ridge shown as *feature 1* in the figure. Viscous impact ejecta deposits (*feature 4* in Figure 3a) derived from a rampart crater (*feature 5* in Figure 3a) are cut by a set of northwest-trending grooves (*feature 6* in Figure 3a). Figure 3a also shows younger craters postdating the grooves (*feature 7*) and wrinkle ridges (*feature 8*). Figure 3b is a zoomed-in view showing that the steep walls of a set of northeast-trending grooves (*features 1* and *2*) are cut by a north-trending, arcuate-shaped wrinkle ridge (*feature 3*); this again supports the view that the groove formation predates wrinkle-ridge formation.

A more complicated relationship between grooves and wrinkle ridges is shown in Figure 3c. Here, a north-trending wrinkle ridge (*feature 1*) splits into three shorter ridges (*features 2a, 2b*, and *2c*) aligned obliquely in an *en echelon* pattern. The ridge system cuts across an east-trending groove that displays an apparent right-separation offset (*feature 3*). The right-separation and the *en echelon* pattern of the minor terminating wrinkle ridges are consistent with right-slip shear, as shown in Figure 3c. The superposition of a younger wrinkle ridge (*feature 4*) over an older east-trending groove (*feature 5*) is also shown in Figure 3c.

The east-northeast-trending bands with eastward pinch-out terminations (*feature 5* in Figure 2c) are broad ridges (*feature 1* in Figures 4a and 4b) that are 40–50 km wide and 40–80 m higher than the surrounding background plains (Figure 4c). The subtle, broad east-northeast-trending ridges are superposed by north- and northeast-trending wrinkle ridges (*feature 2* in Figures 4a and 4b).

In summary, the following older-to-younger sequence of landform-development events can be deduced from the cross-cutting relationships shown in Figures 2–4: (1) the development of the highland terrain in Thaumasia Planum, which we refer to as the Thaumasia plateau in this study; (2) the formation of northeast-, northwest-, and east-trending grooves likely representing extensional structures; (3) the emplacement of east-northeast-trending lava flows; (4) the formation of wrinkle ridges that are superposed on (a) the highland terrain, (b) the lava-flow terrain, and (c) the earlier formed extensional structures; and (5) rampart craters with layered, viscous-flow-like ejecta blankets.

4.2 Morphologies and Geological Context of the Wrinkle Ridges in the Study Area

Eighteen wrinkle ridges can be recognized in the central area of the 800-km-wide Solis Dorsa basin (Figures 5a and 5b). In map view, individual ridges are 350–400 km long and 10–20 km wide. The ridges display arcuate and convex-eastward traces (Figure 5a) and occur on both the western and eastern slopes of the Solis Dorsa basin while maintaining the same convex geometry (Figures 5a and 5b). In cross-section view, the center-to-center distances of the ridges mostly fall between 50 and 70 km. The amplitudes of the ridges vary from ~100 to ~250 m (Figures 5b and 5c).

In the study area, we mapped six wrinkle ridges, numbered wr1 to wr6 in Figures 5a and 5c. The geological context of the six ridges was defined by mapping over a CTX image superposed over a THEMIS nighttime temperature map. Our mapping revealed the following landform units (Figure 6): (1) craters that do not have direct cross-cutting relationships to the wrinkle ridges (unit *ct*), (2) craters that postdate the wrinkle ridges (unit ct_2), (3) wrinkle ridges (unit *wr*), (4) craters with their impact ejecta-blanket deposits cut by ridge-bounding faults (unit ct_1), (5) darker toned bands with digitate margins (unit *bd*), and (6) lighter toned background terrain that hosts the darker toned bands (unit *pl*). Examples of craters postdating and predating wrinkle ridges are shown in Figure 7.

Excluding the overlapping images, 16 HiRISE images were available in the study area for detailed examination of landforms associated with the wrinkle ridges and inter-ridge plains. We refer to each HiRISE image strip as an investigation site, numbered from 1 to 16 (Figure 6a). Figure 8 shows that wrinkle ridges in the study area are covered extensively by boulders, which are best exposed where the fine-grained mantling material is absent. The images in Figure 8 also show parallel and evenly spaced ridges and grooves, which are together referred to as striations for their resemblance to striations on fault surfaces. Note that the center of each HiRISE image in Figure 8 is also shown by the *x* and *y* coordinates, that are displayed when the images are viewed using the HiVivew software.

Meter-scale boulders are also scattered across the plains between wrinkle ridges (Figure 9). Linear landforms composed of light-toned and fine-grained materials with grain sizes below the resolution of HiRISE images occur widely on the surface of the boulder-bearing inter-ridge plains (Figure 9). These linear features are likely eolian bed forms, which differ from the linear grooves and ridges on top of the wrinkle ridges in that (1) the boulders are not aligned linearly and no well-defined grooves are found next to the light-toned ridges, and (2) the striations on ridge tops trend northwest, whereas the light-toned ridges on the plains trend northeast.

The largest craters in the inter-ridge plains display layered, viscous-flow-like ejecta-blanket deposits (Figures 10a, 10b, 10d, and 10e). The exposed crater walls on the inter-ridge plains show well-defined bedding (Figures 10c and 10f). One of the largest craters on top of the wrinkle ridges is shown in Figures 10g and 10h. This crater differs from those exposed on the inter-ridge plains in that

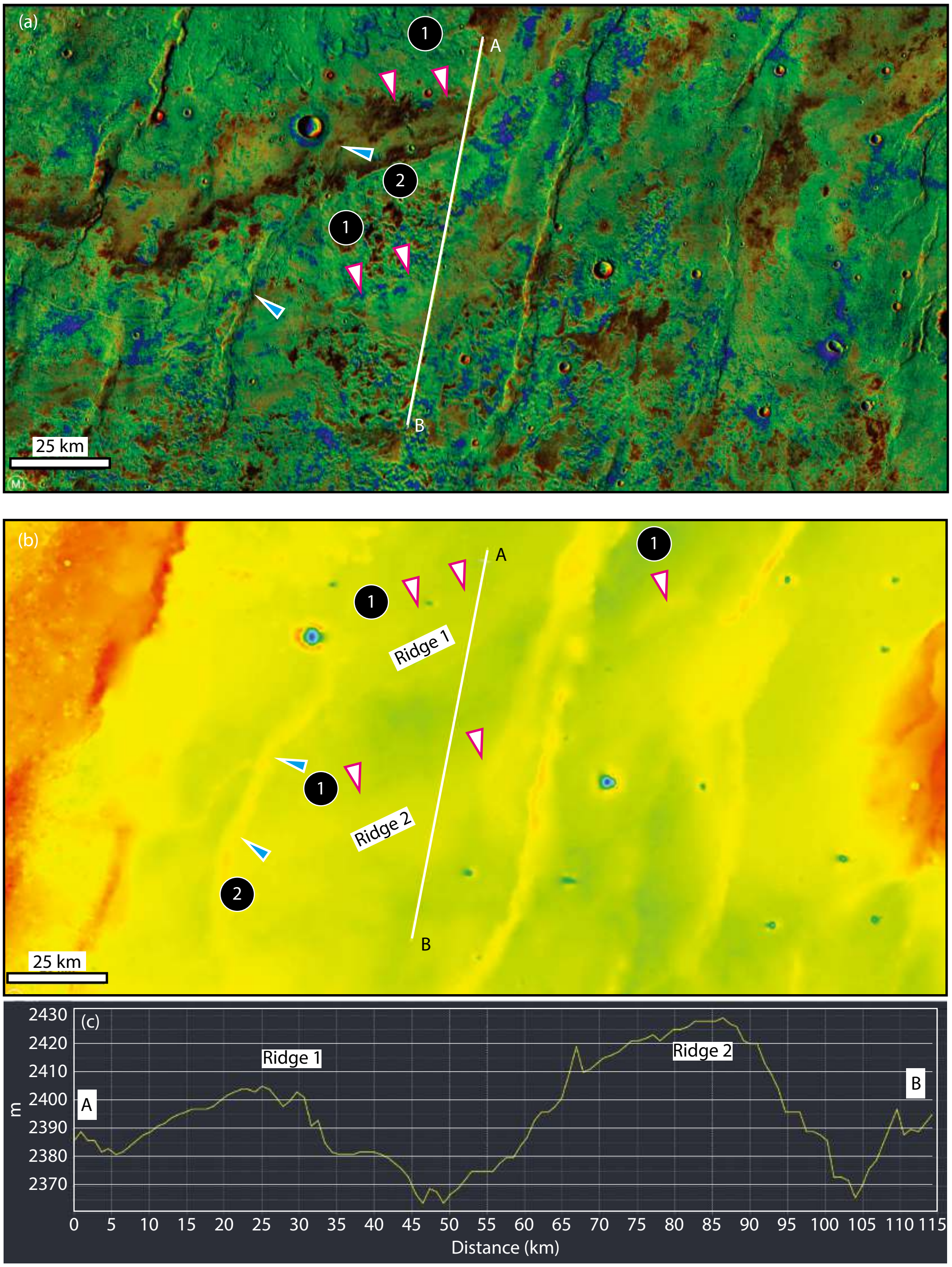

Figure 4. (a) A colored nighttime temperature map that is blended with a THEMIS image, a CTX image, and a shaded digital elevation model (DEM) relief map. Numbers on the image mark the locations of the geomorphological features mentioned in the text. The white straight line A–B marks the topographic profile shown in panel (c). (b) A DEM map of the same area shown in panel (a), with blue arrows pointing to wrinkle ridges and white arrows pointing to the east-trending, lower relief ridges marked by darker and lighter toned bands in the nighttime temperature map. The ridges are interpreted as lava flows (see text for details). The letters A–B mark the location of the topographic profile shown in panel (c). (c) Topographic profile along a line across the east-trending ridges. See panel (c) for location.

(1) it does not display viscous-flow-like ejecta deposits, (2) the crater wall displays only three well-defined bedding horizons and the rest appear to be massive-textured materials, (3) the crater floor exhibits a lobate ridge with a northward-concave shape that requires a northern source, and (4) no landslide scarps are present on the northern crater wall that rule out the lobate ridge having resulted from mass wasting.

The wrinkle ridge traversed by investigation sites 2, 3, and 4 (Figure 6) displays several types of lobate landforms. The western edge of the ridge is marked by a lobate apron sheet (Figures 11a and 11d), a lobate taper (Figures 11b and 11e), and a lobate ridge

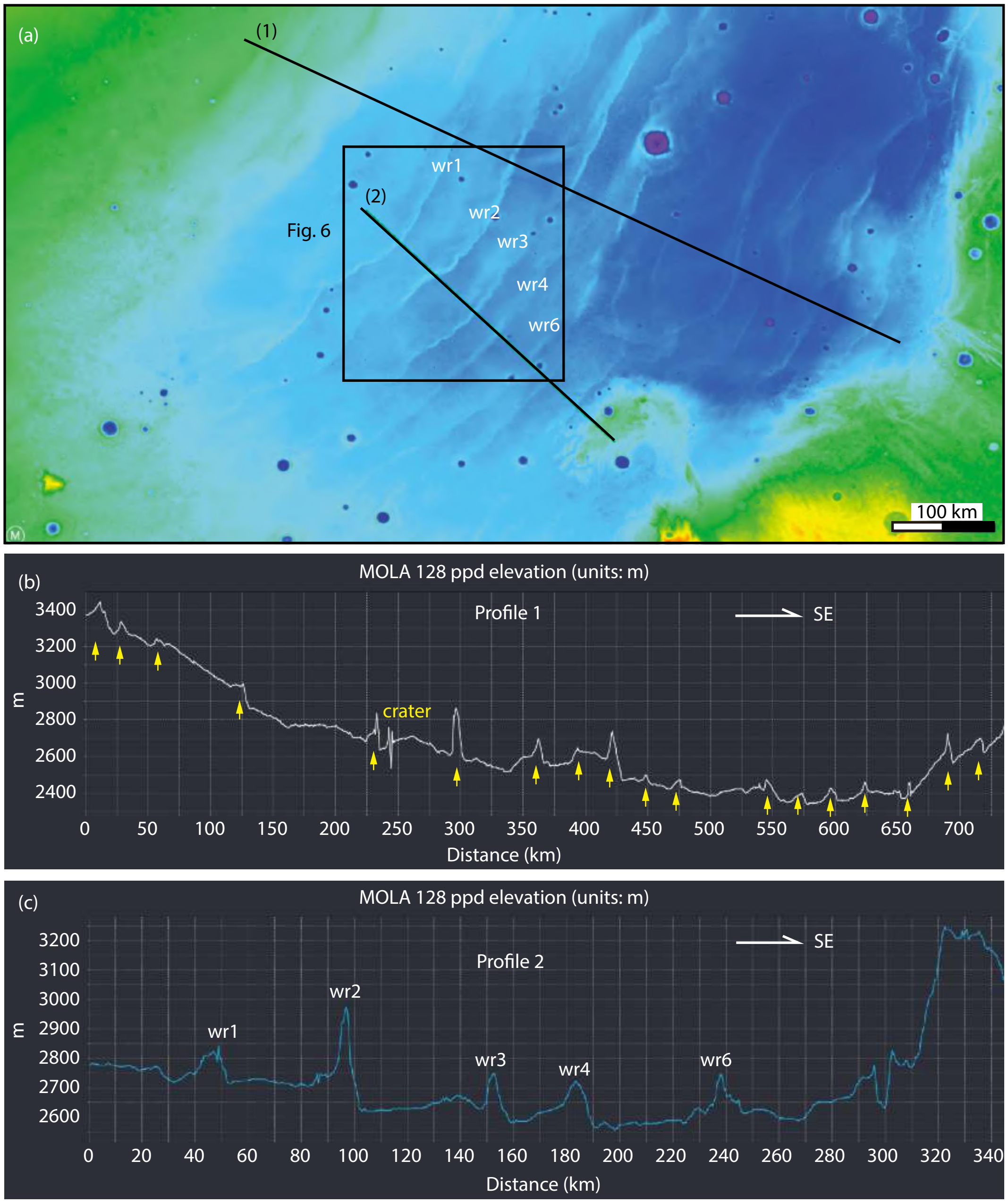

Figure 5. (a) Digital elevation model map of the Solis Dorsa wrinkle ridge field and the locations of profiles 1 and 2 shown in panels (b) and (c). Also shown is the location of Figure 6a. (b) Topographic profile across the entire Solis Dorsa wrinkle ridge field. Yellow arrows indicate the locations of wrinkle ridges in the cross section. (c) Topographic profile across the study area in the southern part of the Solis Dorsa wrinkle ridge field.

(Figures 11c and 11f), respectively. The lobate apron sheet is superposed on top of the wrinkle ridge (Figure 11a). Similarly, the lobate taper composed of massive-textured boulder-bearing materials is piled on top of the flat wrinkle-ridge surface (Figure 11b). Less prominent is the lobate ridge that lies on top of the wrinkle-ridge surface (Figure 11c). The superposition relationships above suggest that the lobate landforms postdate the formation of the wrinkle ridge. The eastward-convex shapes of the lobate taper and lobate ridge require eastward movement of the taper and ridge materials. However, no candidates are present as the pushers because these landforms lie against the flat inter-ridge plains to the west (Figures 11b and 11c). The eastern front of the same wrinkle ridge is also marked by lobate landforms, which are expressed as arcuate-shaped, flow-front-like steep limbs (Figures 11a–11c). In all three cases, the steep ridge fronts transition to flat ridge tops through round-shaped hinge zones (Figures 11a–11c).

Boulder-bearing ridges occur widely in the study area. The best exposed ridge network is at site 7 on the inter-ridge plains (Figure 12). The ridges display crude dendritic-network patterns with ridges merging or converging northeastward. Zoomed-in views show that the ridges are composed of boulder materials that are locally layered, dipping to the northeast in the direction of ridge convergence (Figures 12b–12d). Note that the strike of the inclined beds in Figure 12d trends perpendicularly to the nearby

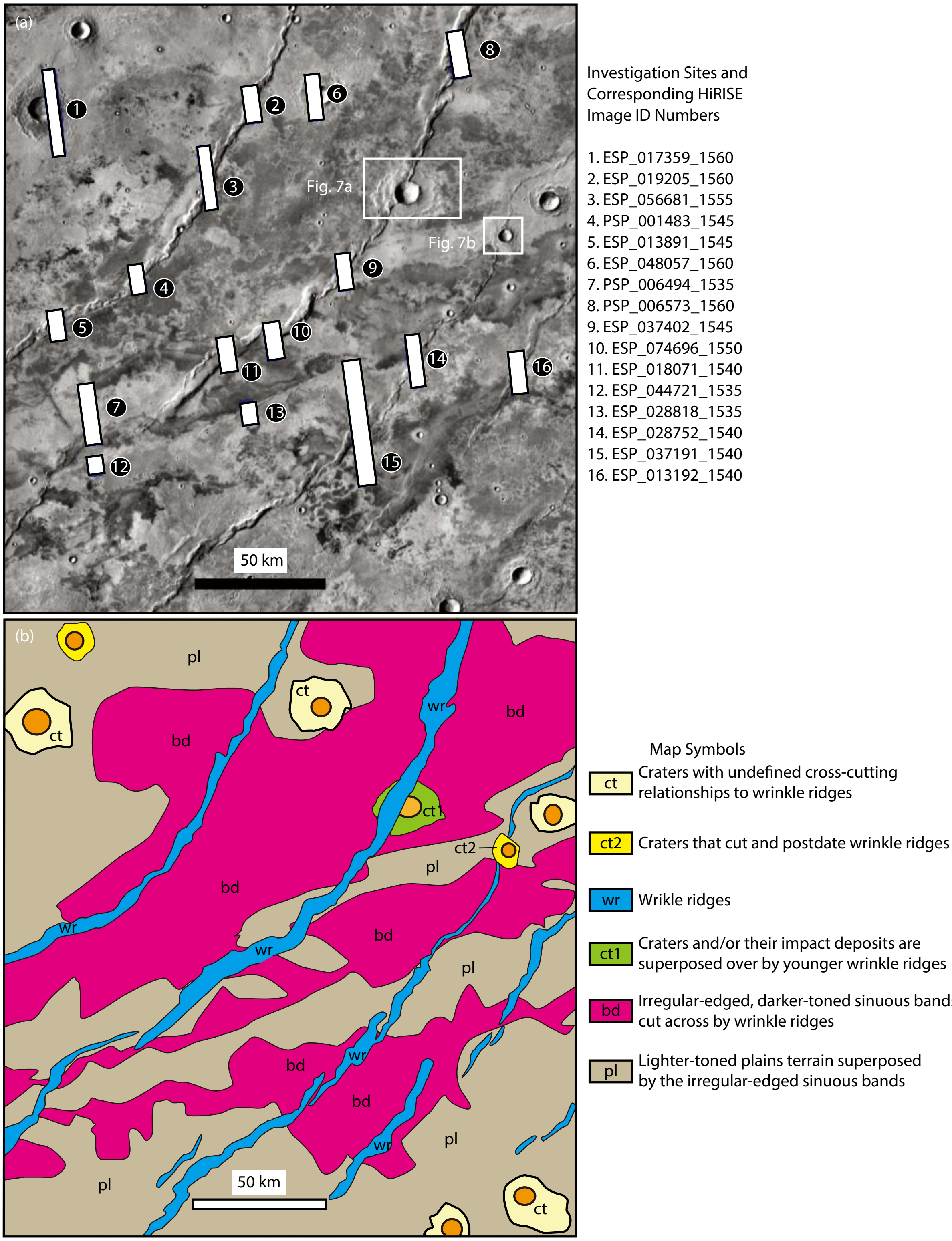

Figure 6. (a) A black-and-white nighttime-temperature THEMIS image blended with a CTX image, and a digital elevation model shaded relief map. Numbers next to the white boxes are referred to as investigation sites in this study, which correspond to the locations of the analyzed HiRISE images, with their identification numbers indicated on the side of each image. (b) Geomorphological map of the same area shown in panel (a) that shows the relationships among the interpreted lava flows expressed as irregularly shaped, sinuous bands (unit *bd*), wrinkle ridges (unit *wr*), and the background plains terrain (unit *pl*). See map legend and text for a more detailed description of the mapped units.

wrinkle ridges. As discussed hereafter, the smaller ridges hosting inclined beds may have been formed as glacial eskers, and the dipping beds are cross-beddings. In this interpretation, the bed dip direction indicates northeastward flow, which is consistent with the flow direction required by the northeastward convergence of the minor ridges that host inclined beds.

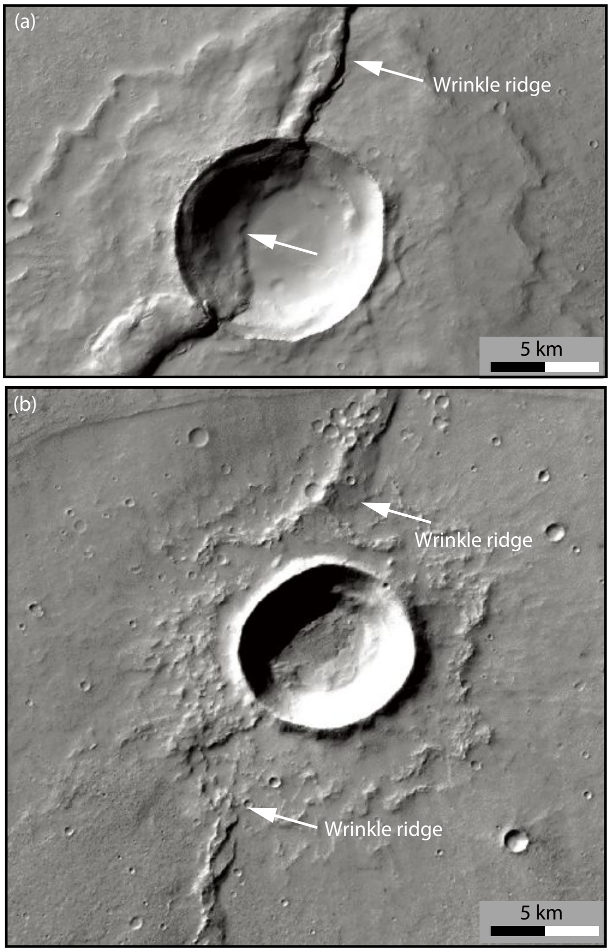

Figure 7. (a) A CTX image that shows a wrinkle ridge cutting across an impact crater. (b) A CTX image that shows an impact crater terminating a wrinkle ridge. See Figure 6a for the locations of the two images and the text for details.

4.3 Detailed Mapping of Site 11

Investigation site 11 is covered by HiRISE image ESP_018071_1540 at a resolution of 50 cm/pixel. We mapped this site systematically (Figure 13) to establish the spatial distribution of secondary landforms associated with larger wrinkle ridges and the chronological relationships between the secondary landforms and the hosting wrinkle ridges. We divided the map area into three geomorphological assemblages: the northern plains, the wrinkle ridge, and the southern plains.

(1) Northern Plains Assemblage. This assemblage consists of a single unit: rough-surfaced plains terrain (unit *rf* in Figure 13b). This unit is characterized by patches of flat, higher elevation mesa surfaces (*feature 1* in Figure 14a) that are surrounded by depressions of similar sizes (*feature 2* in Figure 14a). This terrain also exposes degraded, polygonal-shaped craters characterized by breached crater rim ridges (*feature 1* in Figure 14b) with flat crater floors (*feature 2* in Figure 14b). Knobs surrounded by smooth-surfaced plains are also present (*feature 3* in Figure 14b). Finally, viscous-flow-like landforms without a clear association with the nearby impact craters occur locally in this terrain (*feature 4* in Figure 14b). Even the crater with a better preserved rim ridge has a smooth-surfaced flat crater floor (*feature 1* in Figure 14c) similar to those of the degraded craters. This observation implies that the process responsible for flat crater-floor development occurred after the emplacement of the two types of craters. The wall of the crater shown in Figure 14c exposes meter-sized boulders without discernible layering (*feature 1* in Figure 14d). The rim ridge and the wall of the crater are superposed by northwest-trending linear ridges and grooves (*feature 2* in Figure 14d). The smooth-surfaced material on the crater floor embays the crater-wall boulders (*feature 3* in Figure 14d), suggesting that the formation of the flat crater floor postdates the formation of the crater. The most characteristic feature in the rough-surfaced plains terrain (*feature 1* in Figures 14e–14g) is boulder piles of various shapes that are superposed by fresh (*feature 2* in Figures 14e–14g) and degraded craters (*feature 3* in Figures 14e–14g).

(2) Wrinkle-Ridge Assemblage. This assemblage displays the most diverse landforms in the mapped area. On the northern and southern margins of the wrinkle ridge are the northern and southern foothill terrains (unit fh_N and unit fh_S in Figure 13b), which are characterized by (1) scarp-bounded, uneven-surfaced, wrinkle-ridge-parallel highland strips and (2) discontinuous, round-topped ridges that are parallel or oblique to the main trend of the wrinkle ridges. The main part of the wrinkle ridge is divided by a curvilinear-ridge terrain (unit *cr* in Figure 13b) into the northern and southern smooth-surfaced ridge terrains (unit sr_N and unit sr_S in Figure 13b). A lumpy-ridge terrain (unit *lr* in Figure 13b) lies between the northern rough-surfaced plains terrain and the northern smooth-surfaced ridge terrain. Finally, irregularly shaped depressions with flat floors and steep walls (unit *ird* in Figure 13b) are present in the northern part of the wrinkle ridge.

The landform units mentioned above are superposed by (1) linear and curvilinear scarps best developed along the northern and southern margins of the wrinkle ridges, although some isolated scarps also occur on top of the smooth-surfaced ridge terrain (purple lines in Figure 13b), and (2) sinuous, sharp-crested ridges (light orange lines in Figure 13b).

Figure 15a shows the locations of zoomed-in images of the wrinkle-ridge landform assemblage. Figure 15b shows a scarp-bounded, uneven-surfaced highland strip in the northern foothill terrain (*feature 1*). A zoomed-in view of the highland strip shows that it exposes meter-sized boulders expressed as dark- and light-toned dots (*feature 1* in Figure 15c). The base of the southern scarp in Figure 15c displays eolian bedforms (*feature 2*). Figure 15d shows the curvilinear, sharp-crested ridges on top of the wrinkle ridge, whereas Figures 15e–15g are zoomed-in views of the ridges that expose massive-textured boulder materials. Note that dendritic patterns of ridge networks are indicated in Figure 15e (*feature 1*), which are embayed by the younger, smooth-surfaced mantling material (*feature 2*). Materials making up the wrinkle ridge are exposed by the crater walls (Figures 15h–15j), which do not show clearly defined layering. The flat ridge top shows distinctive regions with (*feature 1* in Figure 15k) or without (*feature 2* in Figure 15k) the fine-grained mantling materials.

The southern foothill terrain has a transitional boundary to the southern plains assemblage, as shown in Figure 16a. Key morphological features of the southern foothill terrain are shown in Figures 16b–16e. Figures 16b and 16c show a foothill characterized

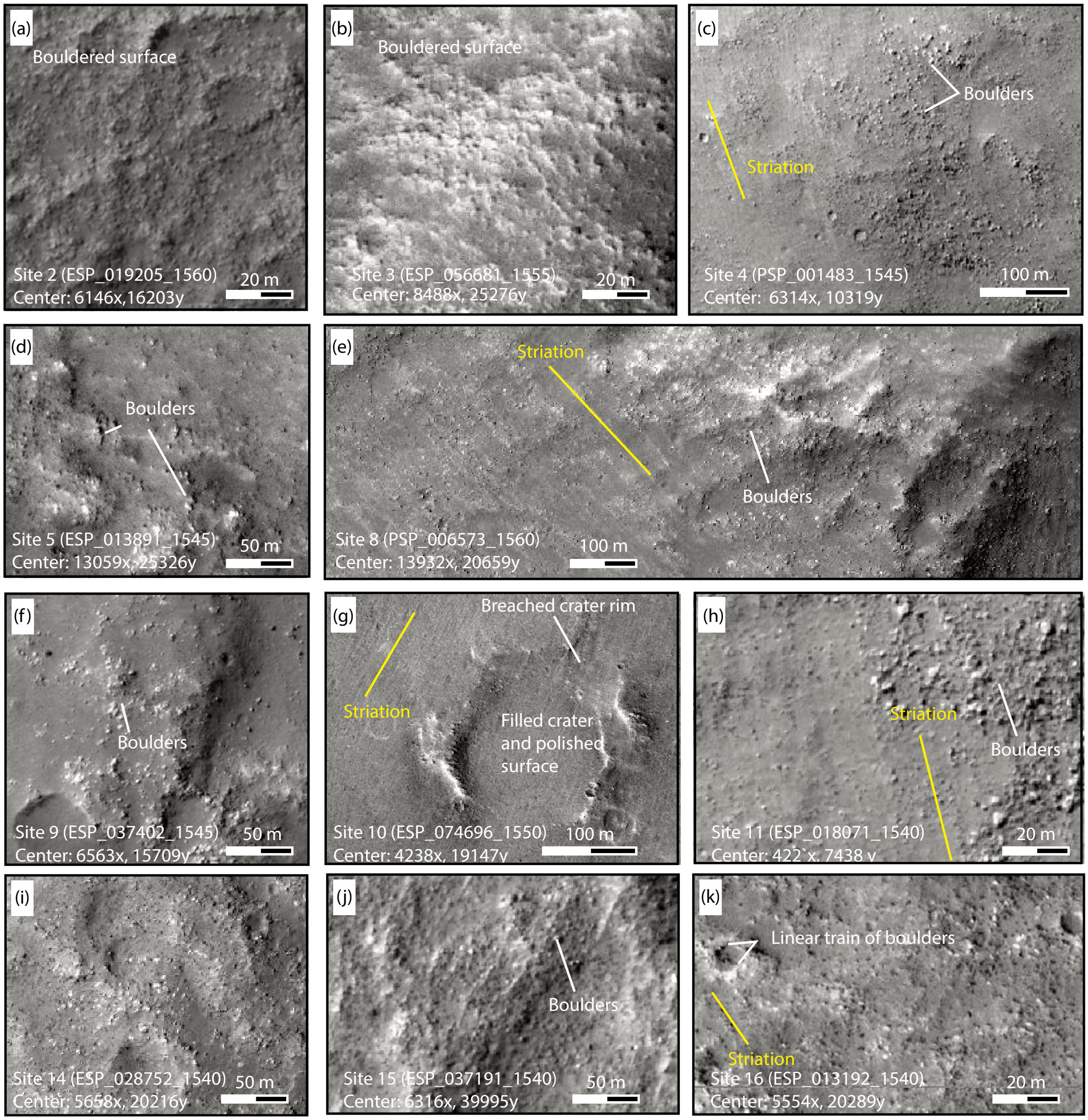

Figure 8. (a–k) Zoomed-in HiRISE images that show boulder-bearing surfaces, striated surfaces on top of the mapped wrinkle ridges, or both. The site number and the HiRISE identification number are indicated on each image and correspond to those listed in Figure 6. See text for details.

by a sharp crest and bounded by a steep south-facing scarp (*feature 1*), which bounds a smooth-surfaced basin to the north (*feature 2*) that lies at higher elevation than the plains (*feature 3*) south of the sharp-crested ridges. The sharp-crested ridges in the foothill terrain are locally highly curvilinear and perched on a south-facing slope (*feature 1* in Figure 16d). Both the ridge and the hosting slope expose meter-sized boulders (*feature 2* in Figure 16d).

Irregularly shaped mound complexes are also present in the southern foothill terrain (*feature 4* in Figure 16b). A zoomed-in view of a mound complex shows a sharp-crested ridge (*feature 1* in Figure 16e) that truncates a circular depression resembling a degraded impact crater (*feature 2* in Figure 16e). The younger ridge material is also emplaced into the crater basin crater (*feature 3* in Figure 16e). Note that the geomorphological relationship shown in Figure 16e is similar to those shown in Figure 11, which resemble gravel piles pushed up by bulldozers. Here, we refer to this class of landforms as "bulldozed-pile-like" features.

Note that the sinuous ridge in the southern foothill terrain is remarkably similar to the map-view traces of the ridge shapes in the curvilinear ridge terrain (Figure 16i; cf. Figures 15d–15g). A zoomed-in image shows that the ridge is composed of layered boulders (Figure 16j). Similar to the internal layered structure shown in Figure 12d, the strike of the inclined beds in Figure 16j is orthogonal to the trend of the nearby wrinkle ridges. As discussed above for the ridges in Figure 12d, inclined beds may have been formed within glacial eskers, and the dipping beds may represent cross-beddings. In the glacial-esker interpretation, the northeast dip of the cross-beddings indicates northeastward flow of water and sediment transport.

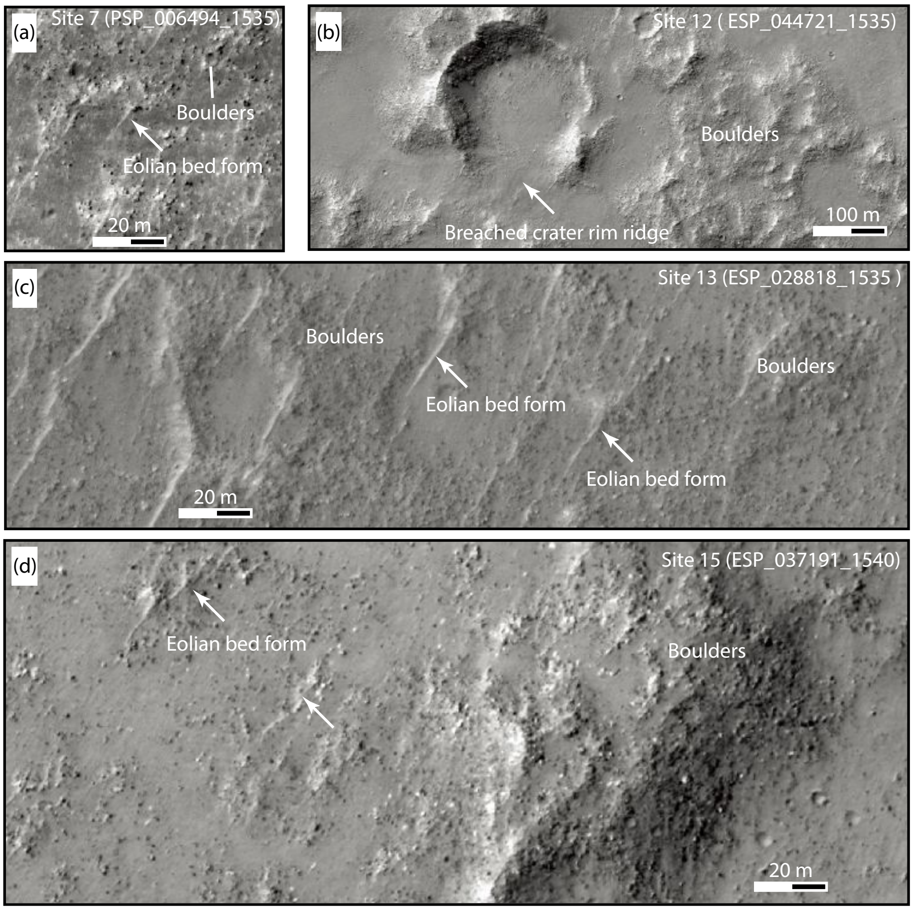

Figure 9. (a–d) HiRISE images that show boulder-bearing surfaces, light-toned eolian bed forms, and breached crater rim ridges exposed on the inter-ridge plains. The site number and the HiRISE identification number are indicated on each image and correspond to those listed in Figure 6. See text for details.

(3) Southern Plains Assemblage. This assemblage consists of a smooth-surfaced plains terrain (unit *sf* in Figure 13b) and a rough-surfaced plains terrain (unit *rf* in Figure 13b). The smooth-surfaced plains are characterized by the presence of light-toned mantling materials that fill the lowland regions including craters (*feature 1* in Figure 16f). In contrast, the rough-surfaced plains terrain is free of the mantling materials despite its occurrence next to the smooth terrain (*feature 2* in Figure 16f). The rough-surfaced plains expose meter-scale boulders on a surface that is dotted by degraded craters (Figure 16g), whereas the smooth-surfaced plains lack the appearance of boulders because of the presence of the mantling materials (Figure 16h).

In addition to the three assemblages mentioned above, we also mapped two other types of landforms: striations and scarps (Figure 17). The northwest-trending striations are expressed as linear, regularly spaced, parallel boulder ridges (*feature 1* in Figure 17b) and flat-floored grooves (*feature 2* in Figure 17b). The surface that hosts the striations appears to have been polished, which is expressed by the occurrence of flat-rimmed craters (*feature 3* in Figure 17b).

The northwest-facing scarp (*feature 1* in Figure 17c) bounding a northern foothill of the wrinkle ridge (see Figure 17a for location) against the northern plains truncates an arcuate ridge on the flat top of the foothill (*feature 2* in Figure 17c). This relationship indicates the scarp formed after the foothill.

The foothills along the northern margin of the wrinkle ridge are composed of boulders (Figure 17d). The scarp that bounds the boulder hill in Figure 17d (*feature 1*) is locally collapsed because of mass wasting, forming a talus pile that buries the scarp below (*feature 2*).

Figure 17e shows a crater rim ridge (*feature 1*) that is truncated by an east-facing scarp (*feature 2*). Note that the scarp material intrudes into the crater basin (*feature 3* in Figure 17e). Also note that the impact deposits recognizable below the scarp (*feature 4* in Figure 17e) are missing on top of the flat-topped ridge above the scarp.

Figure 17f shows a flat-floored depression (*feature 1*) that is truncated by an east-facing scarp (*feature 2*). The scarp exposes parallel linear ridges and grooves (*feature 3*), which may represent inclined layers dipping to the northeast. The observed inclined beds are similar in bed thickness to and share the same northeast dip direction as the inclined beds shown in Figure 12d. Similar to the internal layered structure shown in Figure 12d, the strike of the inclined beds in Figure 17f is orthogonal to the trend of the nearby wrinkle ridges. As discussed above for the ridges in Figures 12d and 16j, inclined beds may have been formed within glacial eskers, and the dipping beds may represent cross-beddings. In the glacial-

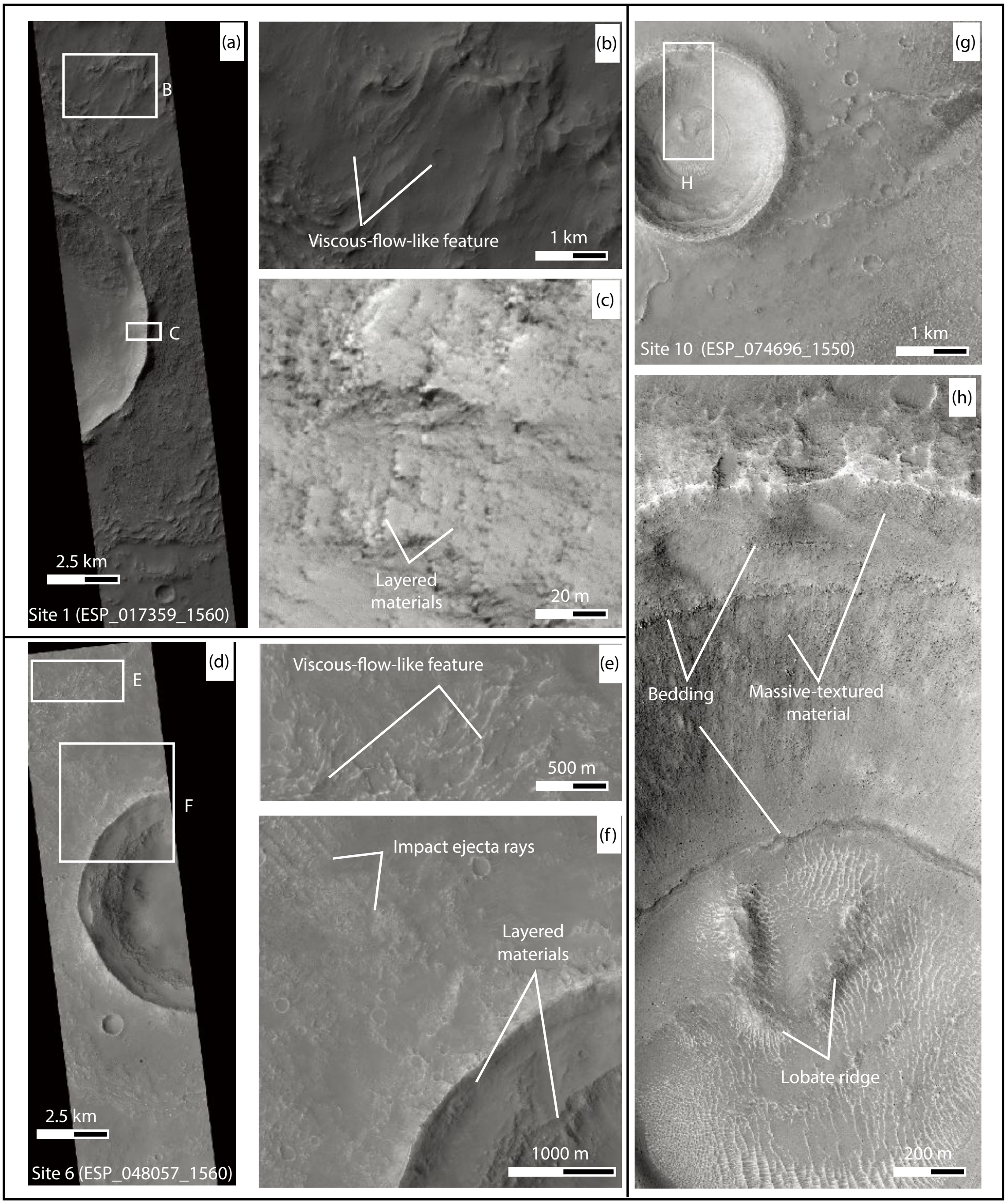

Figure 10. HiRISE images of craters mapped in Figure 6. (a) An overall view of the images shown in panels (b) and (c). (b) A viscous-flow-like feature that is a part of the impact ejecta blanket of a rampart crater. (c) Bedding exposed on a crater wall. (d) An overall view of the image shown in panels (e) and (f). (e) Viscous-flow-like features as a part of the impact ejecta blanket from a rampart crater. (f) Impact ejecta rays from a crater. Also shown is bedding on a crater wall. (g) Bedding exposed on a crater wall. (h) A close-up view of weathering-resistant beds on a crater wall. Also shown is a lobate ridge on the crater floor.

esker interpretation, the northeast dip of the cross-beddings shown in Figure 17f indicates northeastward flow of water and sediment transport.

We interpret the ridges in Figure 17f as representing a glacial esker and the inclined beds as cross-bedding bed forms. The shared dip direction to the northeast, as shown in Figures 12d and 17f, indicates a regional northeast subglacial flow.

On the basis of the geological mapping, we discuss the possible sequence of geological events in the study area. The light-toned mantling material has filled both degraded and relatively well-preserved crater basins in the northern plains terrain (Figure 14). In contrast, the mantling material in the southern plains covers only the smooth-surfaced plains terrain, where craters and depressions are filled by this material (Figures 16f and 16h). The rough-surfaced plains terrain, on the other hand, lacks the mantling material even though it can lie (e.g., *feature 2* in Figure 16f) directly adjacent to the smooth-surfaced plains terrain

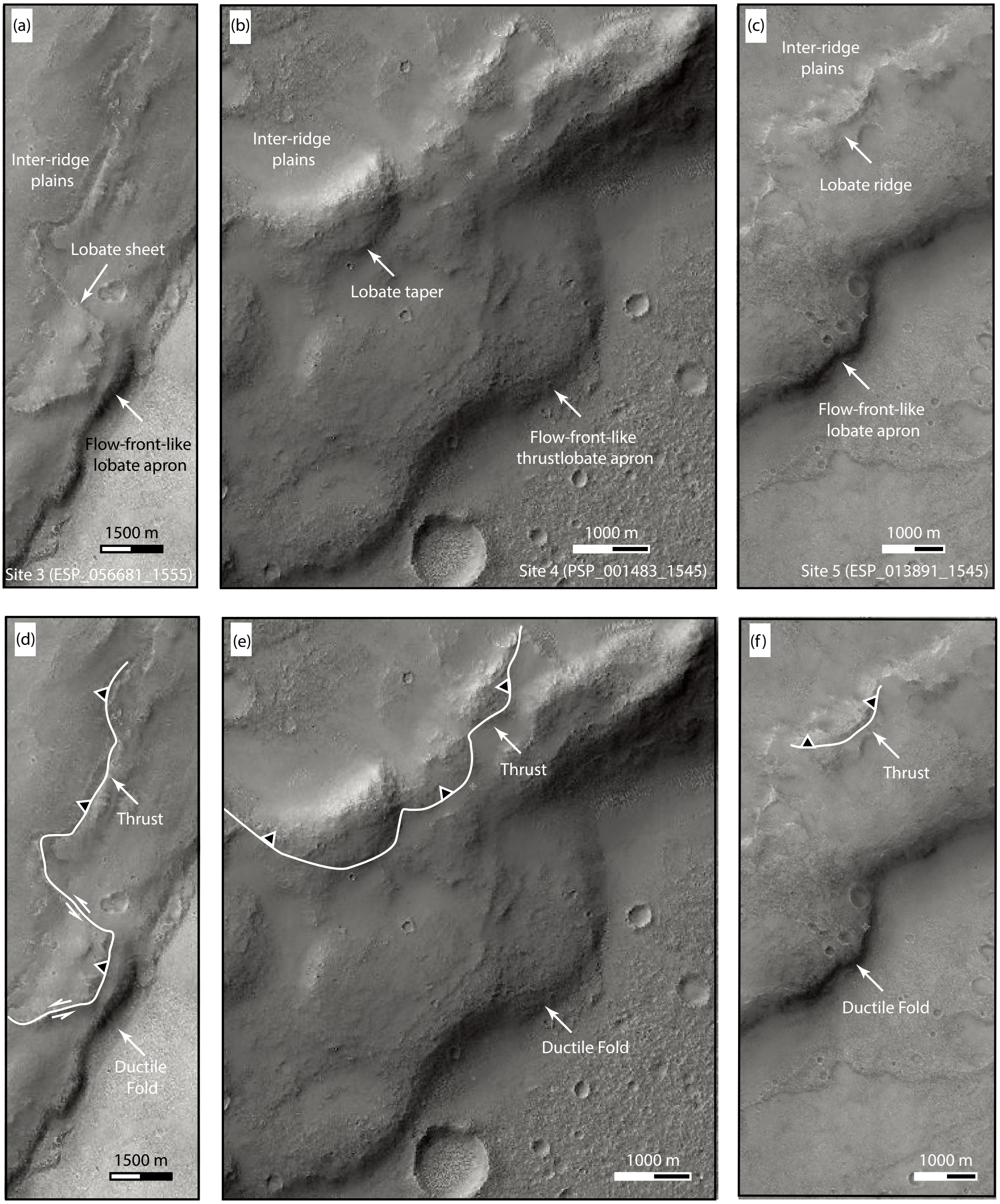

Figure 11. HiRISE images that show lobate-apron-like landforms with lava-flow-front-like margins. Also shown are a tongue-shaped sheet in panel (a) and lobate ridges in panels (b) and (c). The site number and the HiRISE identification number are indicated on each image and correspond to those listed in Figure 6. (d–f) Interpreted outlines of the key geomorphological features shown in panels (a) to (c).

covered by the mantling material (e.g., *feature 1* in Figure 16f). Note that sharp boundaries between regions with and without the mantling material also occur on top of the wrinkle ridge (see Figure 15k). The age relationship between the smooth-surfaced and rough-surfaced terrains in the plains and ridge regions has two possible interpretations. First, the formation of the rough-surfaced terrain may have occurred after the emplacement of the mantling material. However, the similar elevation and the lack of a clear topographic break between the two terrains make this interpretation unlikely. Second, the emplacement of the mantling material is spatially heterogeneous; areas covered by the materials display a smooth-surfaced texture, whereas areas not covered show the original rough-surfaced texture. Because the mantling material occurs on top of the ridge and on the ridge-bounding plains, its emplacement must postdate the wrinkle-ridge formation.

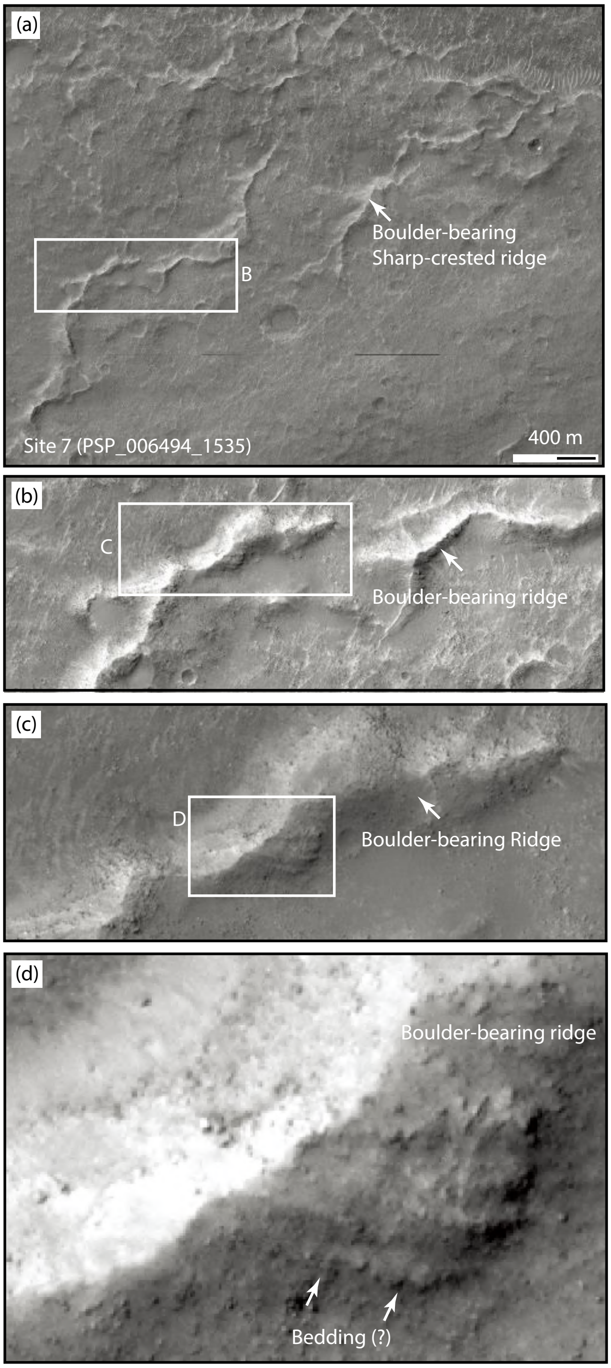

Figure 12. HiRISE images of sinuous, sharp-crested, boulder-bearing ridges on top of a wrinkle ridge. The site number (i.e., site 7) and the HiRISE identification number (i.e., ESP_048057_1560) are indicated on the image and correspond to the same numbers shown in Figure 6. (a) Sinuous, sharp-crested, boulder-bearing ridges and ridge networks atop a flat wrinkle ridge. Also shown is the location of panel (b). (b) A close-up view of boulder-bearing ridges and the location of panel (c). (c) A zoomed-in view of the same boulder-bearing ridge shown in panel (b) and the location of panel (d). (d) Meter-sized boulders defining inclined layers exposed on the ridge side.

Geomorphological features that formed after the wrinkle-ridge formation include (1) the set of northeast-trending linear grooves on top of the wrinkle ridge (black lines shown in Figure 13b) and (2) the sharp-crested, curvilinear, and locally dendritic-patterned ridge networks (light orange lines in Figure 13b). Note that the curvilinear-ridge terrain truncates the northwest-trending linear grooves (Figure 13b), which implies that the emplacement of the boulder-bearing, sharp-crested, curvilinear ridges occurred after the wrinkle-ridge surface was grooved. Also note that the grooves are filled by the mantling material, which implies that the mantling event postdates the grooving event. Because the curvilinear, sharp-crested ridges are embayed by the younger mantling material, the ridge formation predates the mantling event.

In summary, our mapping reveals the following sequence of events in the study area: (1) formation of the main wrinkle ridges and their foothill terrains, (2) formation of the northwest-trending grooves on top of the wrinkle ridges, (3) formation of boulder-bearing, curvilinear, sharp-crested ridges, and (4) emplacement of the heterogeneously distributed mantling material.

Our work indicates that the scarp formations postdate their bounded ridges; their truncation relationships with early landforms, such as curvilinear ridges and impact craters, require the scarps to represent fault-like deformation structures. The occurrence of parallel ridges and grooves on a polished surface suggests that the surfaces of the mapped wrinkle ridges had been modified by younger erosional events capable of shaping the alignment of meter-scale boulders.

5. Discussion

Our regional and local geologic mapping and our systematic analysis of HiRISE images and HRSC topographic data led to the following first-order observations:

(1) The northeast-trending wrinkle ridges with reliefs of 100–300 m (Figure 5) in the Solis Dorsa area are superposed on older east-trending, lower relief (<30 m) ridges (Figure 4). The digitate margins, sinuous and winding traces, and eastward-converging terminations (Figures 3, 4, and 6) all support the view that the older east-trending ridges were formed by eastward downslope-flowing basalt-lava flow.

(2) In map view, individual wrinkle ridges display consistent eastward convex shapes (Figure 5a), which implies an eastward transport direction of the landform system, as it represents a thin-skinned fold-and-thrust belt (e.g., Allemand and Thomas, 1995; Karagoz et al., 2022a, b; cf. Mueller and Golombek, 2004).

(3) In cross-section view, the wrinkle ridges occur on the two sides of the Solis Dorsa basin, with the basin margins sloping to the east in the west and to the west in the east (Figure 5b).

(4) Wrinkle ridges either cut across craters (Figure 7a) or are cut by craters (Figure 7b).

(5) The surface of the wrinkle ridges and their bounding plains expose massive-textured, meter-sized boulders (Figure 8).

(6) The boulder-bearing surfaces are locally superposed by parallel, regularly spaced boulder-bearing ridges and grooves (Figures 8c, 8e, 8g, 8h, 8k, and 17b).

(7) Craters with diameters greater than 4–5 km display layered,

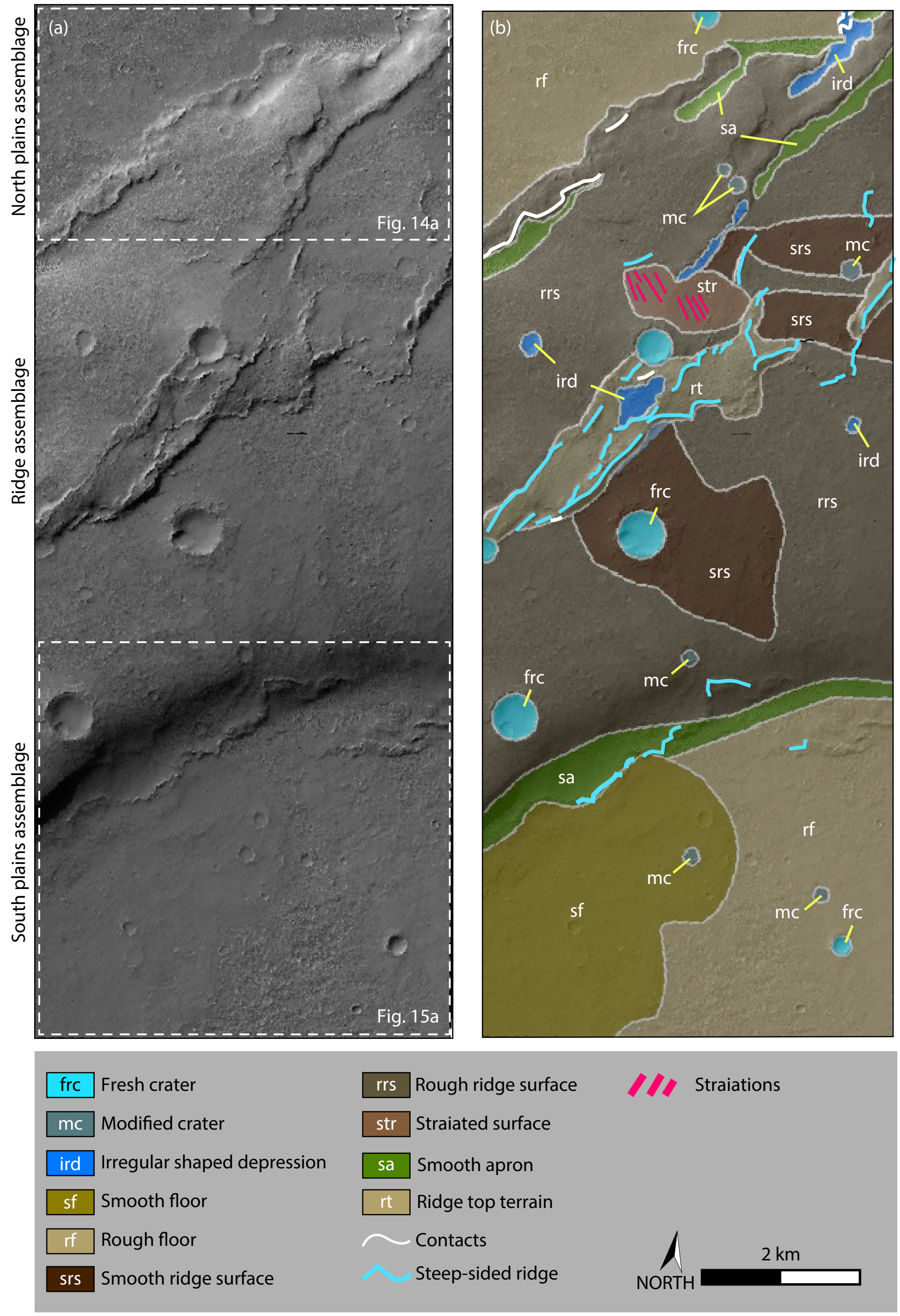

Figure 13. (a) HiRISE image (site 11 and ESP_018071_1540) at a resolution of 50 cm/pixel. The boxes indicate the locations of Figures 14a, 15a, 16a, and 17a. (b) Geomorphological map interpreted from image (a). See text for details.

viscous-flow-like ejecta deposits (Figures 7, 10a, 10b, 10d, and 10e).

(8) The margins of wrinkle ridges locally display flow-like fronts in cross-section view and lobate-apron-like shapes in map view (Figure 11).

(9) A distinctive type of landform was also recognized in this study, which is characterized by a shape resembling debris piles pushed by bulldozers (Figures 11 and 16e).

(10) Wrinkle ridges and their bounding plains are locally superposed by sinuous, sharp-crested, and boulder-bearing ridges (Figures 12, 16c, 16d, and 16i). The ridges locally expose inclined layers dipping consistently to the northeast (Figures 12d, 16j, and 17f).

(11) A light-toned, smooth-surfaced mantling material is draped over most wrinkle ridges and their bounding plains. However, the mantling is not spatially uniform, with some regions directly adja-

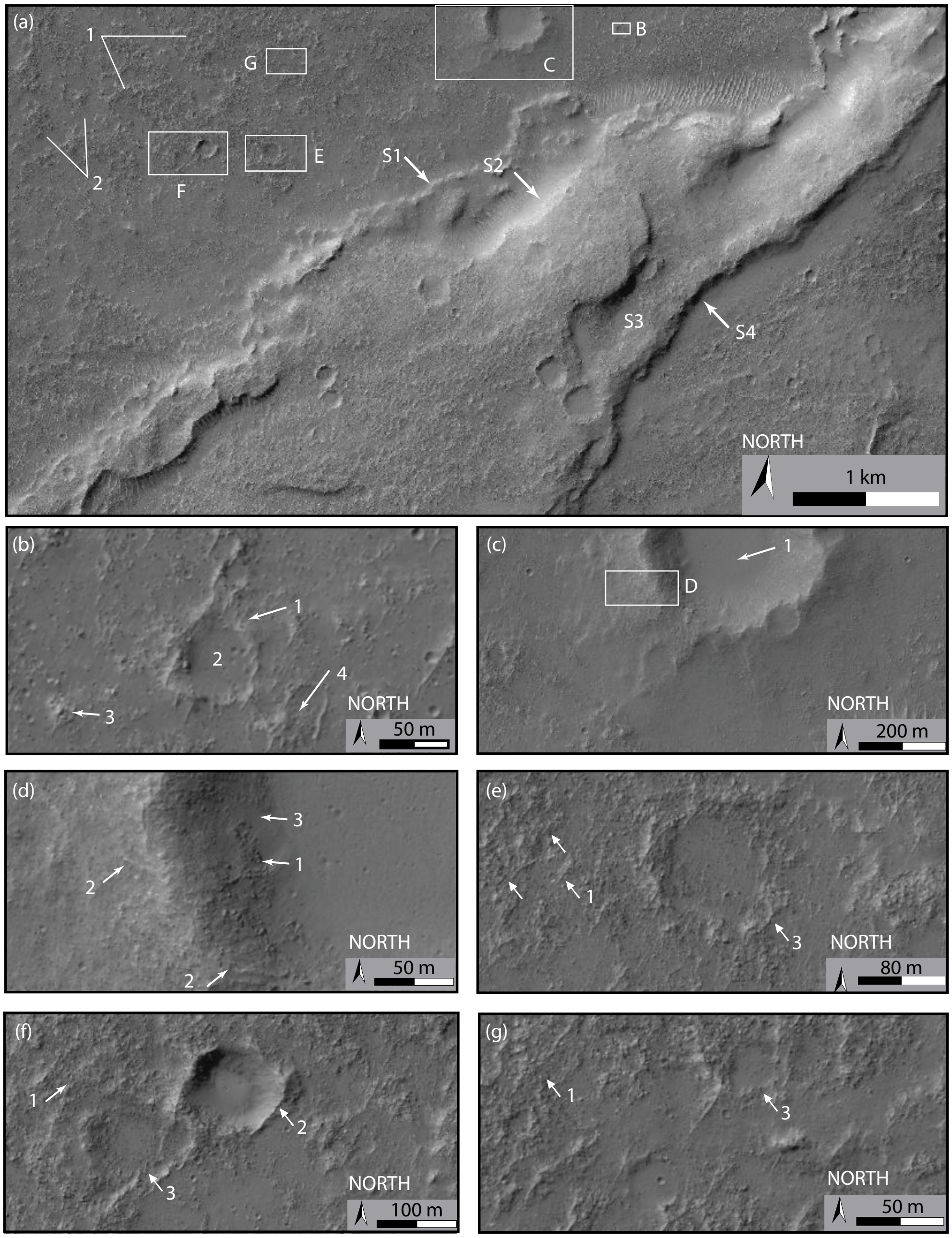

Figure 14. (a) An overview image (site 11 and HiRISE image ESP_018071_1540) of the northern plains. The white boxes indicate the locations of panels (b), (c), (e), (f), and (g), and S1 to S4 mark the mapped scarps shown in Figure 13b. Images (b) to (g) display geomorphological features described in the text.

cent to mantled terrain showing no signs of mantling (Figure 16f).

(12) Our regional (Figure 6b) and local mapping (Figure 13b) led to the following interpreted older-to-younger sequence of events for the landscape evolution of the Solis Dorsa wrinkle ridge field:

(a) The formation of the Thaumasia highlands.
(b) The formation of linear grooves across the highlands.
(c) Emplacement of the east-trending ridges interpreted as lava flows that were stopped in the east by the Thaumasia highlands.
(d) The development of boulder-bearing surfaces on top of the flows.
(e) The formation of wrinkle ridges and coeval impacts that display rampart-style ejecta-blanket deposits.
(f) The development of striated surfaces over wrinkle ridges and inter-ridge plains. Degraded craters could also have been formed during this time.
(g) The development of sinuous, sharp-crested, and boulder-bearing ridges that locally expose inclined beds.
(h) The spatially heterogeneous distribution of mantling material that fills older craters.
(i) The formation of modern eolian landforms best expressed as dune fields in lowland regions and depressions.

Any models for the formation of wrinkle ridges and their subsequent modifications in the Solis Dorsa region must account for the observations above and have a self-consistent geologic

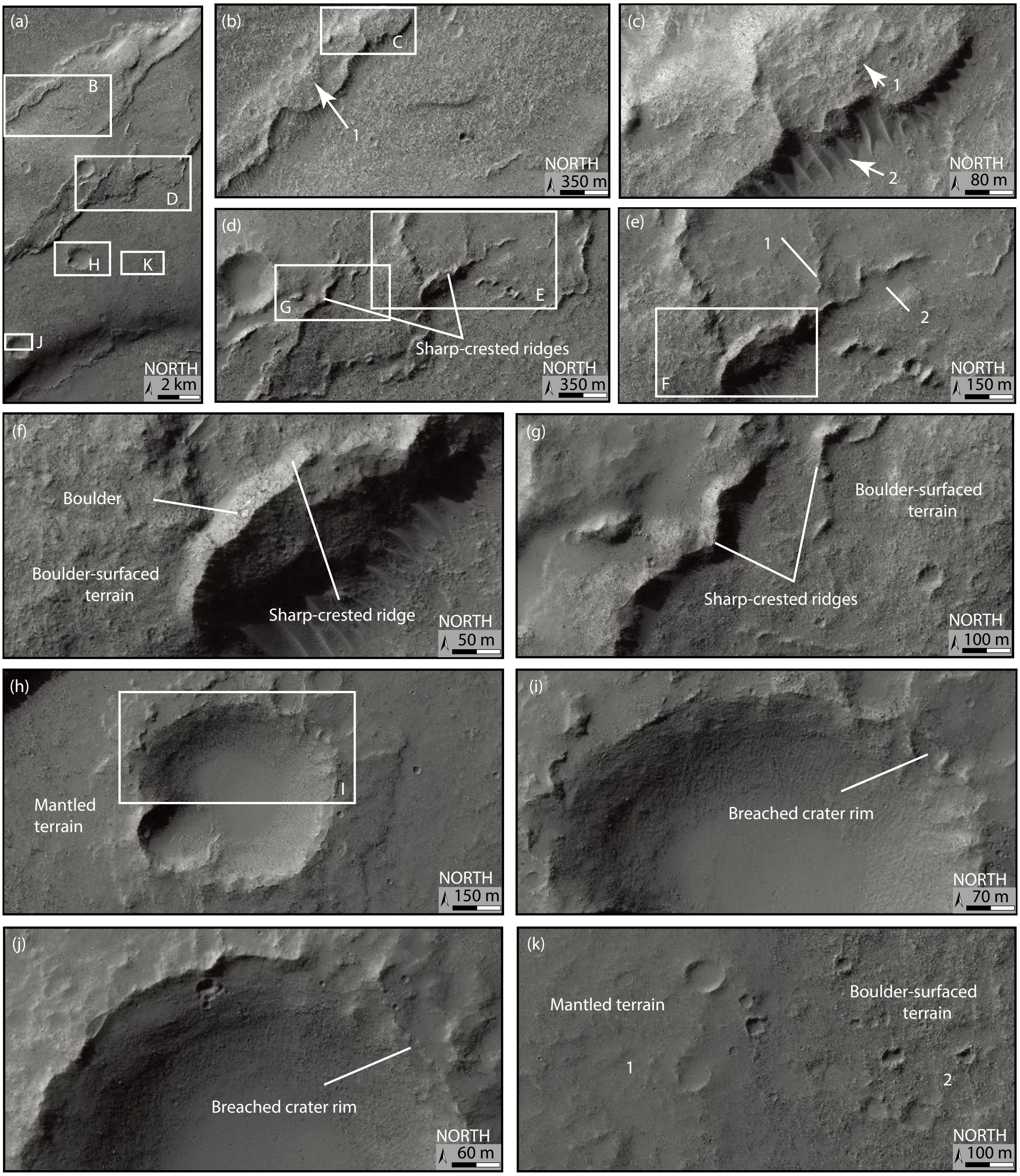

Figure 15. (a) An overview image (site 11 and HiRISE image ESP_018071_1540) of the southern plains. The white boxes indicate the locations of panels (b), (d), (h), and (k). Images (b) to (k) show geomorphological features described in the text.

history as constrained by our mapping.

5.1 Origin of Surficial Boulders

Meter-scale boulders that occur everywhere in the regional study area could have been generated by three possible processes: (1) impact gardening that resulted in the formation of a surficial boulder-bearing regolith layer (e.g., Hartmann et al., 2001; Warner et al., 2017; Figure 18a), (2) autobrecciation of volcanic flows (e.g., Parsons, 1969; Smellie et al., 2011; Figure 18b), and (3) glacial tills (e.g., the subglacial stone pavement of Hicock, 1991, and the glacial-boulder pavements of Atkins, 2013; Figure 18c) (Also see Kakaria and Yin, 2023).

The impact gardening model predicts that boulders in the study area should have sizes from <1 m to >100 m, which has been observed on Mars (i.e., the mega-breccias of Grant et al., 2008, and Tornabene et al., 2013). Our observations contradict this expectation; they show instead that the boulder sizes are limited to an upper size limit of ~5 m (Figure 8). Hence, invoking the impact gardening mechanism would require additional processes that helped sort the clast sizes. For example, it is possible that our

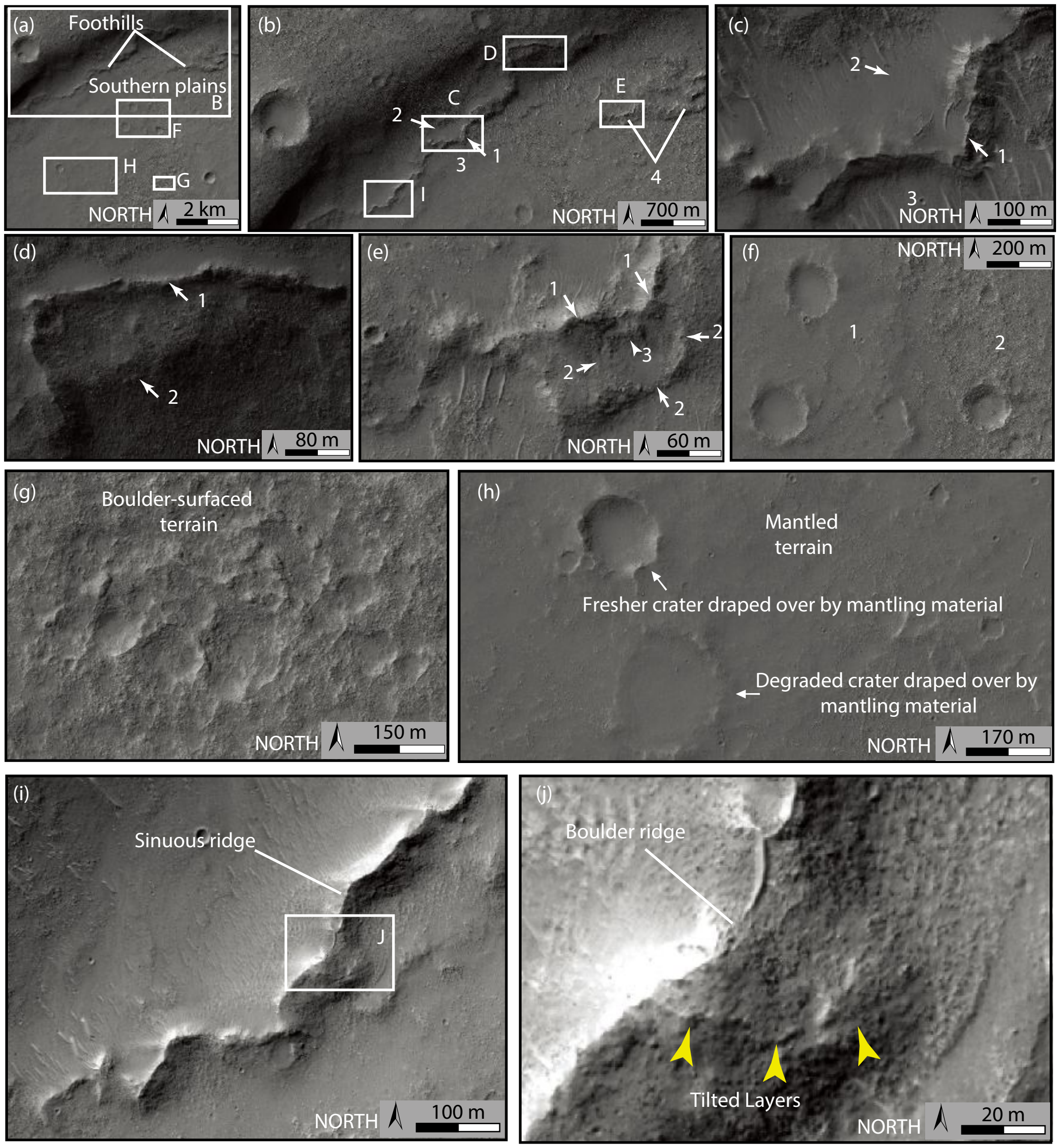

Figure 16. Zoomed-in views from HiRISE image ESP_018071_1540, which show geomorphological features in the southern foothill terrain and the southern plains unit described in the text. Panel (a) provides the locations of panels (b), (f), (g), and (h) in this figure. Panel (b) provides the locations of panels (c), (d), (e), and (i) in this figure. Panel (i) shows the location of panel (j).

study area is located far from large craters capable of creating breccias that are tens of meters across. But this factor alone does not explain why the boulder sizes are generally similar and the upper size limit appears to be similar everywhere in such a large area that is ~300 km wide and 400 km long (Figure 6).

Autoclastic volcanic breccias are those formed (1) within a volcanic plug, (2) at the surface by the rising and crumbling of domes and spines, and (3) within unconfined lava flows (Parsons, 1969). Flow breccias may develop on top of a lava flow, resulting in the formation of aa-type surface textures (Parsons, 1969). This interpretation is consistent with the presence of interpreted lava flows in the area. One observation this hypothesis may not be able to explain is the occurrence of rampart craters with viscous-flow-like ejecta deposits in areas where wrinkle ridges are developed. Craters with viscous-flow-like ejecta are considered to have been formed in impact-target rocks that contain ice layers (e.g., Mouginis-Mark, 1987; Weiss and Head, 2014; Cassanelli and Head, 2019 and references therein). However, the emplacement of lavas would have created steams and phreatic volcanic explosions, leading to the release of water below the lava flows (e.g., Parsons, 1969; Smellie et al., 2011; cf. Cassanelli and Head, 2019).

Debris-covered glaciers (Benn et al., 2012) can account for all the difficulties not explained by the two hypotheses mentioned above. First, glacial transport may provide a sorting mechanism that limits the maximum clast size (Boulton, 1978). Second, the viscous-flow-like materials could have been derived from the ice layer below the debris layer, as suggested by Cassanelli and Head (2019). A key difference between our debris-covered glacier model and the supraglacial lava-flow model of Cassanelli and Head (2019) is that our debris layer lies above rather than below a lava pile; our model implies post-lava glaciation, whereas their model requires syn-lava glaciation.

The possibility that the surficial boulder layer in the Solis Dorsa

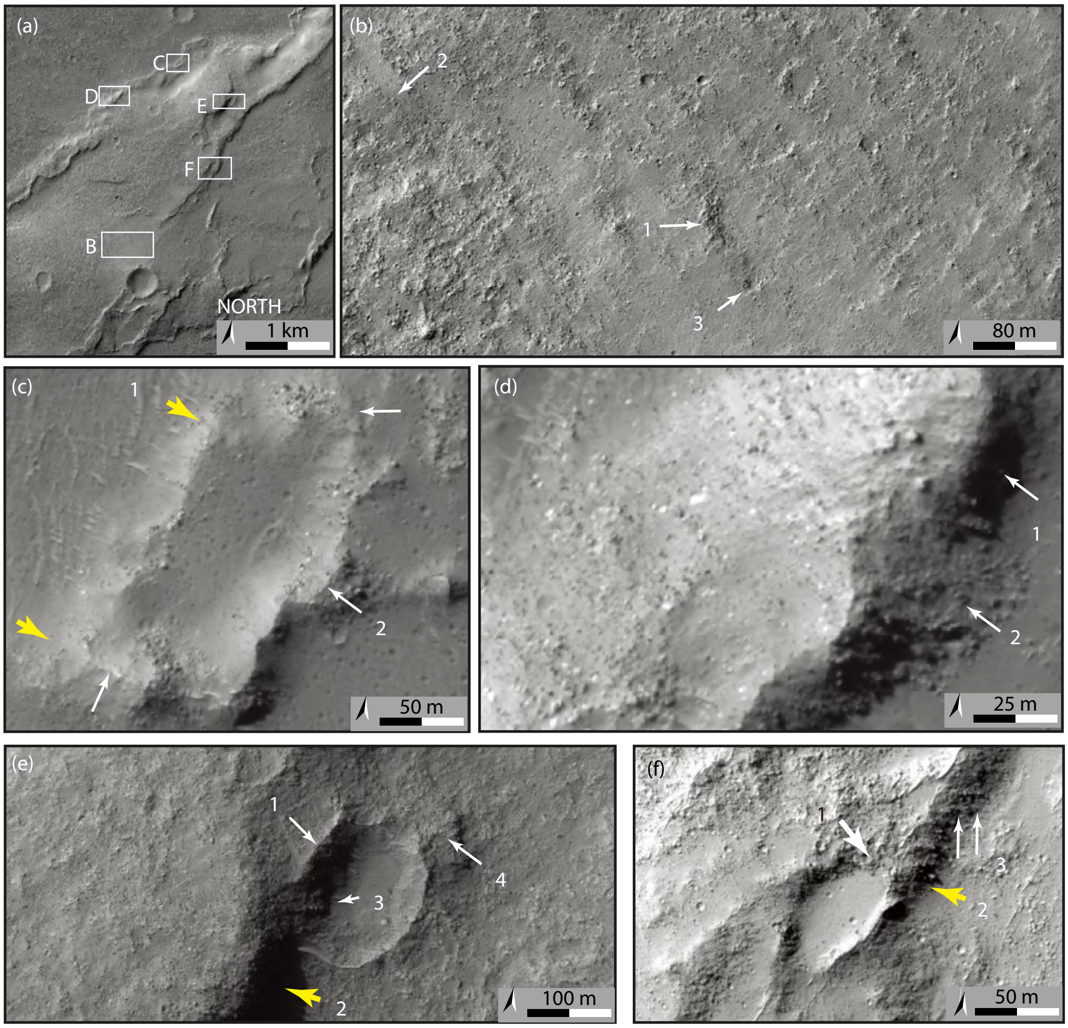

Figure 17. Striations, scarps, and scarp-truncated craters. Panel (a) provides the locations of panels (b) to (f) in this figure. See text for details.

area may represent glacial deposits raises the question of whether the entire wrinkle ridge is made up of allochthonous materials transported by glaciers or whether the ridges are mostly composed of the eastward-trending lava flows and only their surfaces are draped over by a thin (<10–30 m) layer of boulders. As shown in Figure 4a, the nighttime isothermal bands are superposed over most of the wrinkle ridges, which suggests that the major mass of the wrinkle ridges still records the thermal properties of the interpreted lava flows. Hence, we concluded that the wrinkle ridges are not composed of exotic materials except in their surficial layers, which are too thin to alter the thermal properties of the lava flows below.

5.2 Formation Mechanisms of Wrinkle Ridges

As reviewed in Section 1 of the paper, debates on wrinkle-ridge formation have been focused on (1) igneous versus tectonic processes, (2) thermal contraction versus tectonic compression, and (3) crustal-scale, thick-skinned shortening versus shallow-crustal, thin-skinned or décollement-facilitated shortening (see reviews by Mueller and Golombek, 2004, and Watters, 2022).

Igneous mechanisms predict the wrinkle ridges to have formed above an elongated laccolith sheet, which would predict extension and the formation of tensile fractures along the ridge crests (Strom, 1972). The predicted extensional fractures were not observed in this study. However, the flow-front morphology associated with many wrinkle ridges in the study area (Figure 9) does suggest that the formation of the wrinkle ridges may have been accomplished by a ductile-deformation process rather than by a brittle faulting process. We ruled out ductile deformation as having been associated with the lava-flow emplacement because the northeast trend of the wrinkle ridges is oblique rather than perpendicular to the longitudinal east trend of the interpreted lava flows.

Thermal contraction may explain horizontal shortening across the wrinkle ridges. However, this mechanism does not explain why the wrinkle ridges have a consistent eastward-convex shape across the Solis Dorsa wrinkle field. One would also expect that thermal contraction caused by magma cooling below the Tharsis rise would have generated a crustal-scale stress field, leading to the formation of compressional structures with horizontal wavelengths similar to the thickness of the Tharsis crust on the order of tens of kilometers. This expectation is inconsistent with the highly localized deformation expressed by the wrinkle ridges bounded by flat inter-ridge plains (see Karagoz et al., 2022a, b). Finally,

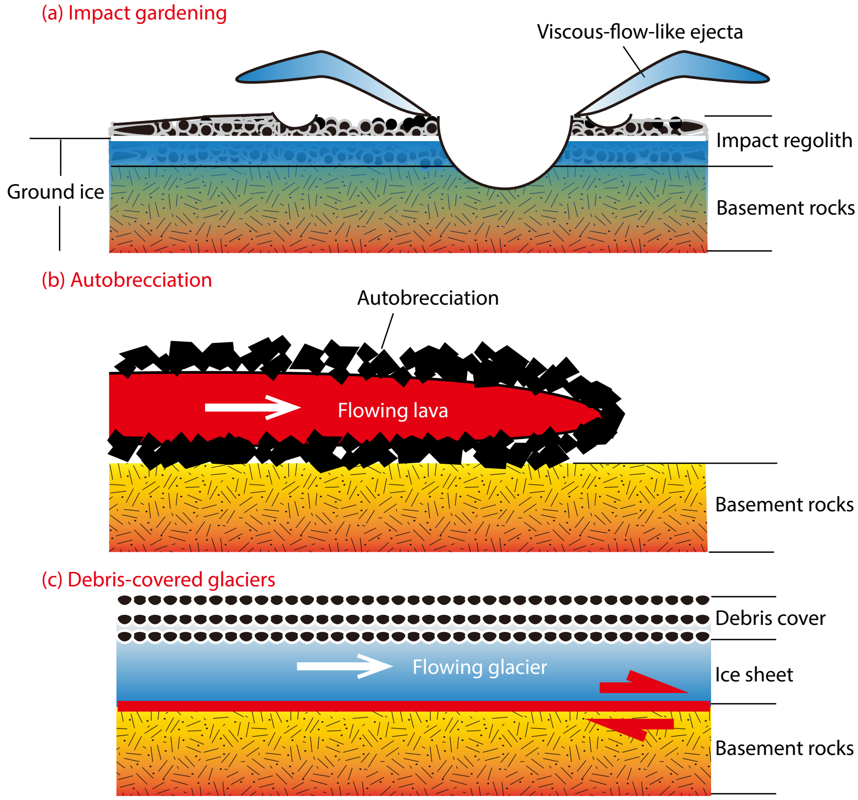

Figure 18. Competing models for the origin of surficial meter-scale boulders across the study area shown in Figure 6: (a) impact gardening model, (b) autobrecciation model, and (c) debris-covered glacier model.

heterogeneous cooling was expected because of multiple intrusions at different times and in different locations below the Tharsis rise, which would require superposition of compressional structures with different orientations that crosscut one another. Such relationships were not observed.

Tectonic compression is a plausible mechanism because it explains the single phase of wrinkle ridge formation, their map-view shapes, and their general parallel relationship to a Himalayan-style mega-thrust that bounds the eastern edge of the Tharsis rise (Nahm and Schultz, 2011). The highly localized topography characterized by wavelengths of only a few kilometers for the ridge width and ridge-bounding plains that have surfaces following the regional slope (Figure 3) is the most consistent with the thin-skinned décollement-fold model, as suggested by Watters (1991) and advocated recently by Karagoz et al. (2022b). In contrast, the thick-skinned thrust model would predict >50-km-wide wrinkle ridges for the faults that terminate at a depth of 30 km with a dip at or below 30°. The >50-km predicted ridge width by the thick-skinned model is incompatible with the observed ridge within the study area (Figure 5).

It is also possible that the wrinkle ridges we mapped were induced by the continental-scale landslide process, as proposed by Montgomery et al. (2009). This model presents two issues. First, the model requires a breakaway zone dominated by normal faults and extensional basins parallel to the wrinkle ridges west of the wrinkle ridge field we mapped. Such a structure has not been recognized in the existing mapping of the region (e.g., Tanaka et al., 2014). Second, the model predicts that the wrinkle ridges would occur only within the landslide block consisting of the southeastern half of the Tharsis rise and in the eastern foreland of the Tharsis rise. However, coeval wrinkle ridges that trend parallel in the north and northeast directions occur within and on all sides of the Tharsis rise (Ruj and Kawai, 2021), which cannot be explained by this model.

A major issue that has not been addressed by either the thin-skinned or thick-skinned décollement-folding model is how the footwall below the décollement is shortened during wrinkle-ridge formation. On Earth, the basement below the décollement folds or thrusts is subducted into the mantle, which is best illustrated by the development of the Canadian Rocky Mountains thrust belt (e.g., Bally et al., 1966; Price, 1981), the sub-Andean thrust belt (e.g., Jordan et al., 1983; McQuarrie et al., 2005), the Zagros fold belt (e.g., Agard et al., 2011), and the Himalayan orogen (Yin A, 2006). Here, we suggest that the basement below the décollement may have been subducted below the warm and ductile root of the Syria volcanic plateau, which is regarded as a magmatic arc created by slab rollback in the primitive plate-tectonics model of Yin A (2012b; Figure 19). This model implies the coeval development of magmatism and wrinkle-ridge formation, which explains the ductile-style folding displayed by the ridges. The model also implies rapid emplacement of lava flows, which allows the development of a ductile décollement at the base of the volcanic pile while under compression.

Although volcanic loading has been proposed as the cause of wrinkle ridge formation (Phillips and Lambeck, 1980), the model predicts downward warping of the lithosphere with extension in

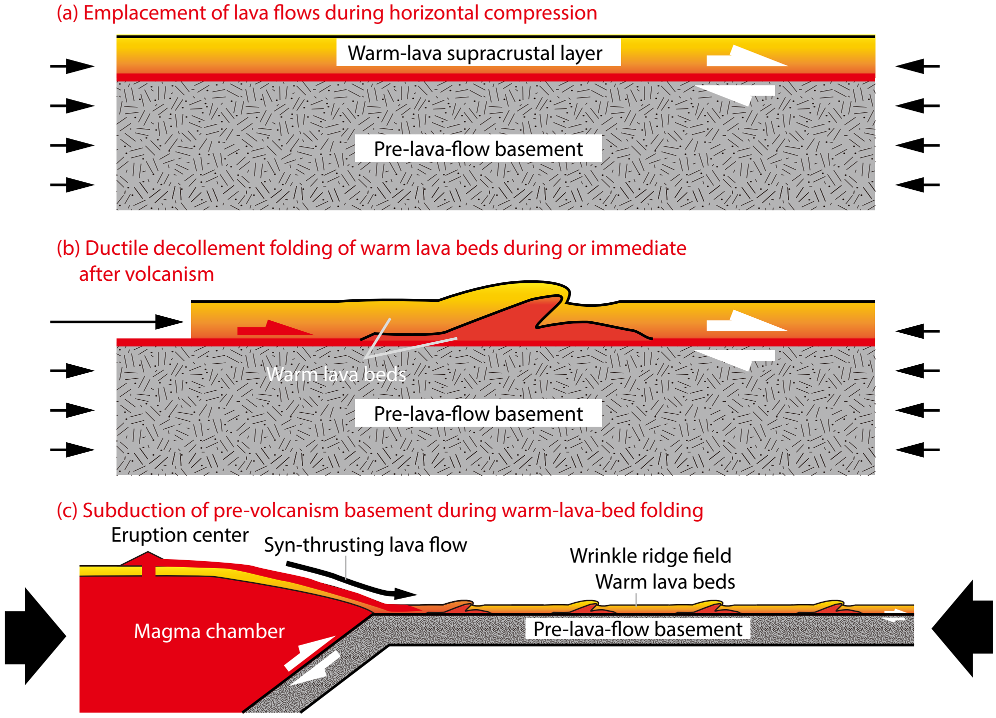

Figure 19. A basement-subduction model for the development of the thin-skinned fold belt represented by the wrinkle ridge field in Solis Dorsa. (a) Emplacement of lava flows coeval with crustal shortening. (b) Ductile folding of warm lava beds in Solis Dorsa. (c) Prevolcanism basement subduction below the ductile root of the volcanic center during the thin-skinned folding of supracrustal lava beds. The upwelling of the hot and ductile lava beds created the flow-front-like morphology of some of the wrinkle ridge margins.

the lower section and extension in the upper section of the lithosphere in cross-section view. In map view, this model predicts compressional structures trending parallel to the margin of the volcanic load, which is the margin of the Tharsis rise. As shown by the regional mapping (Tanaka et al., 2014), wrinkle ridges within and outside the Tharsis rise all trend parallel and are not parallel to the rim of the rise. We note the example that tectonic deformation induced by volcanic loading is the active hot spot in Hawaii. There, the volcanic flank is dominated by extensional faulting, diking, and tensile-fissure development, which are attributed to magmatic push (Yin A and Kelty, 2000), gravitational spreading (Borgia, 1994; Walter et al., 2006), or volcanic-rift spreading (e.g., Morgan et al., 2000; Denlinger and Morgan, 2014). In light of the Earth analogue from the tectonic-deformation pattern in Hawaii, wrinkle-ridge formation could have been related to deep-seated magmatic spreading or shallow-crustal volcanic rifting, or both. This model may explain the wrinkle-ridge formation within the study area inside the Tharsis rise, but the mechanism is incapable of explaining the occurrence of coevally developed parallel wrinkle ridges outside the Tharsis rise. Because of the above-mentioned issues, we tentatively prefer the basement-subduction model for wrinkle-ridge formation, as shown in Figure 19.

5.3 Origin of Boulder-Bearing, Sharp-Crested, Sinuous Ridges, Lobate Ridges, and Rampart Craters

The extreme irregularity of the sinuous ridges in map view and the lack of truncation and offset of craters along the edges of the ridges rule out the possibility that the ridges were formed by horizontal compression during the formation of the hosting wrinkle ridges. Below we consider that the boulder-bearing ridges were possibly formed by (1) weathering-resistant lava tubes (Whitehead and Stephenson, 1998; Orr et al., 2015; Zhao J et al., 2017), (2) inverted fluvial channels (Williams et al., 2009; Zak et al., 2018), and (3) glacial eskers (Shreve, 1985; Clark and Walder, 1994; Warren and Ashley, 1994).

Three observations from the study area contradict the lava-tube ridge observations from the Earth (e.g., Whitehead and Stephenson, 1998; Orr et al., 2015) and Mars; (e.g., Zhao J et al., 2017): (1) the ridges expose meter-sized boulders rather than a coherent lava-flow rock mass, (2) the flanks of ridges are planar and the ridge tops are sharp-crested rather than circular, which is common for lava tubes, and (3) no tumulus breakouts emanating from the ridge flanks were observed. Additionally, we found no collapsed pits and tube-fed lava deltas associated with the boulder ridges as shown to be closely associated with the interpreted lava-tube ridges on Mars (e.g., Zhao J et al., 2017).

Sinuous boulder-bearing ridges could represent inverted fluvial channels supported by their dendritic patterns of ridge networks similar to those exposed on Earth (Zak et al., 2018). However, the lack of ridge-terminating deltaic landforms does not favor this interpretation. Furthermore, the condition for the formation of inverted channels on Earth is that the bounding strata are fine-grained materials easily removable by erosion (e.g., Zak et al., 2018). The scattered boulders next to the boulder-bearing ridges in the study area are not consistent with this prediction. This issue could be overcome if the deltaic deposits and the less resistant finer grained materials originally bounding the channels were completely removed by later erosion. The most challenging issue

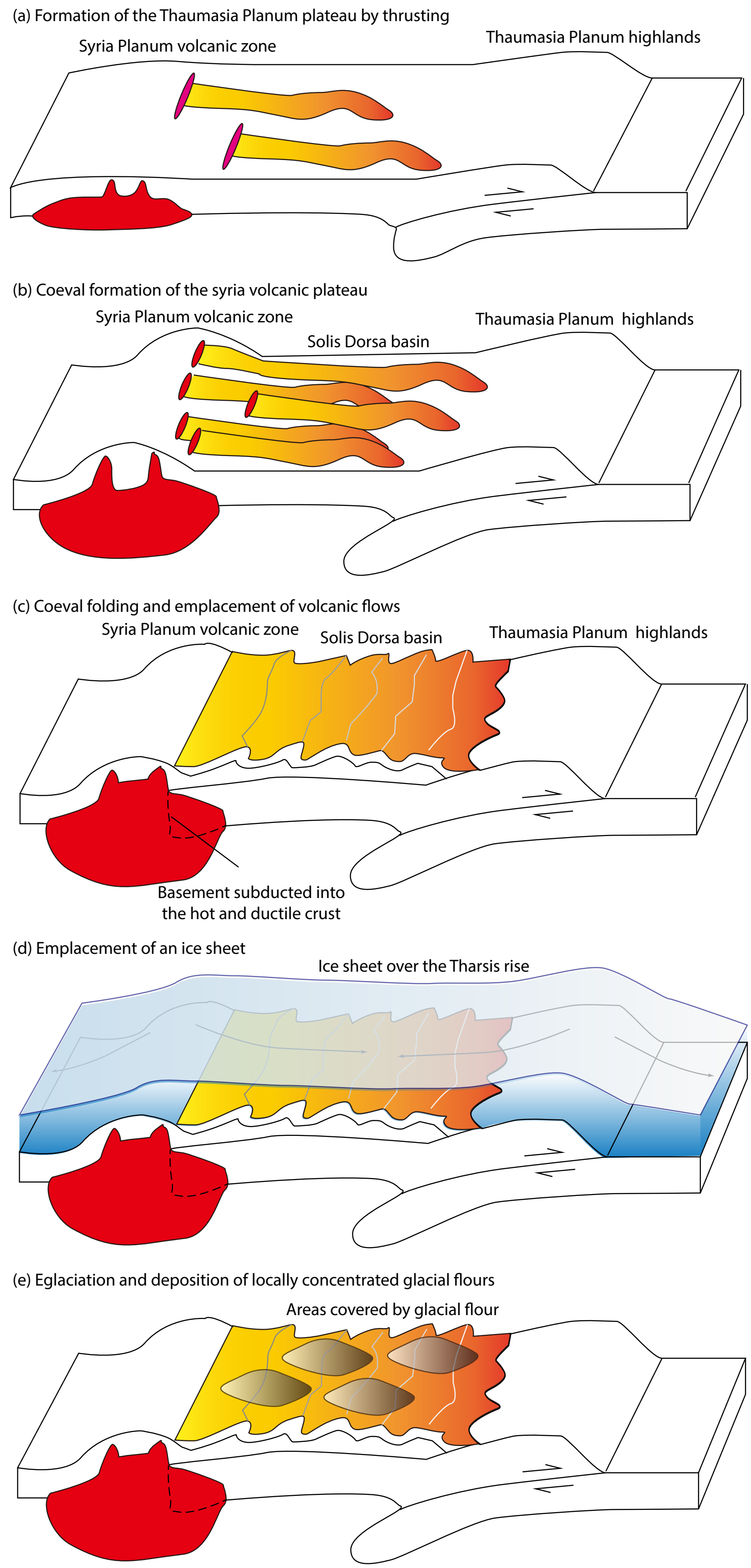

Figure 20. Landscape evolution model of the central and eastern Tharsis rise. (a) Formation of the Thaumasia Planum highlands by thrusting and the coeval development of the Syria volcanic plateau. (b) Continued coeval development of the Syria volcanic plateau and the rise of the Thaumasia Planum highlands. (c) Synchronous folding and eastward emplacement of volcanic flows that filled the Solis Dorsa basin.
(d) Emplacement of an ice sheet over the volcanic pile in Solis Dorsa. (e) Deglaciation and deposition of locally concentrated glacial flours that created mantled terrains.

with the inverted channel hypothesis is that the ridges dominantly trend obliquely to the local maximum slope directions, which is not consistent with their being driven by open-water flow.

Esker-like landforms have been found through Mars (e.g., Kargel and Strom, 1992; Gallagher and Balme, 2015; Butcher et al., 2021). These features do not have to follow the maximum local-slope directions because subglacial meltwater flow is driven by the gradient of hydraulic heads within the overlying ice sheet. This prediction would explain why the boulder ridges trend variably across the study area regardless of the local topography (see Figure 16d for an extreme case). An important implication of the interpretation of this hypothesis for the formation of the boulder-bearing, sharp-crested ridges shown in Figures 12d, 16j, and 17f is that their consistent northeast-dipping beds, interpreted as cross-beddings defined by glacial meltwater-channel deposits, indicate a consistent northeastward subglacial flow direction. Because the hydraulic head is determined by the ice-sheet thickness variation, the interpreted northeast subglacial flow implies a northeastward thinning of the interpreted ice sheet that once covered the study area. It is important to note that the sharp-crested, boulder-bearing, sinuous ridges interpreted as glacial eskers occur on both inter-ridge plains (Figures 12d, 16e, 16i, and 16j) on top of wrinkle ridges (Figure 17f).

Although rare, a single lobate ridge composed of boulders is exposed on a crater floor on top of a wrinkle ridge (Figure 10h). The lack of an escarpment directly above the lobate ridge on the crater wall suggests that it was not formed by a mass wasting process. One possible interpretation is that it represents a terminal moraine. Note that lobate ridges are closely associated with the rampart craters in the area, which have long been considered the result of impacts to ice-bearing targets (e.g., Cassanelli and Head, 2019, and references therein). Here, we suggest that the ground ice is part of the debris-covered ice sheet and that the cover is represented by the widespread deposition of boulder materials after the removal of the underlying ice.

Note that the sequence of geologic events inferred from our study differs drastically from that of Cassanelli and Head (2019). Cassanelli and Head (2019) proposed that the lava flows in the Tharsis region were emplaced while the Tharsis surface was covered by an ice sheet. Their sequence of events was constructed based on inferences from climate modeling and an interpretive synthesis of the existing literature. In our work, we show that the lava emplacement predates the formation of landform assemblages possibly formed by glaciation. Our work, although local in nature, is based on detailed mapping using the highest resolution images available in our study area.

5.4 Striations, Bulldozed Debris Piles, and Irregularly Shaped Depressions

Parallel grooves and ridges defined by the linear alignment of boulders are present throughout the study area. The dominant trend of the linear landforms is northwest–southeast, which is oblique to the trend of the wrinkle ridges. The involvement of boulders with sizes as large as ~5 m rules out the ridge-and-groove formation to have been induced by wind action. The presence of flat-rimmed craters on the polished surface that hosts the linear ridges and grooves supports the interpretation that they were formed by frictional sliding of an overriding ice sheet. Moving glaciers in the study area may also explain the bulldozed debris-pile-like landforms, which appear to have been pushed by strong indenters that were not removed. Glacial push for the formation of this class of landforms resolves this issue.

As shown in the detailed mapping area (Figure 13b), steep-walled, flat-floored, irregularly shaped depressions locally breaching crater rim ridges are present on top of the wrinkle ridges. Although not the focus of this study, similar landforms occur widely on the inter-ridge plains. This class of landforms could have resulted from the melting of dead ice blocks in glacial tills during deglaciation (e.g., Brodzikowski and Van Loon, 1987; Anderson, 1989).

5.5 Why the Mantling Material Is Distributed Heterogeneously

One of the puzzling observations in this study is the highly heterogeneous distribution of the smooth-surfaced mantling material. The filling of this material creates flat-floored craters, and it even partially or completely buries the older craters, as described above. However, directly adjacent to the mantled region is a terrain that displays boulder-bearing surfaces with craters showing no signs of internal fillings and mantling. Because the mantled and unmantled areas lie adjacent to one another on the same surface with the same elevation, it is difficult to attribute the cause of this difference to topography, with the mantling material either transported by wind or falling down as volcanic ash. The aforementioned observation, however, could be explained if glacial flours in the interpreted ice sheet were heterogeneously concentrated. Hence, the deposition of glacial flours from the more highly concentrated portion of the ice sheet resulted in the formation of the mantled terrains, whereas the lack of glacial flours in the overlying ice sheet left the terrain below free of mantling.

5.6 Landscape Evolution Model and Its Implications

On the basis of the discussion above, we propose a self-consistent evolutionary model for the landscape development of the central Tharsis rise.

Stage 1. The Thaumasia plateau was created and uplifted along the eastern margin of the Tharsis rise because of crustal-scale thrusting (Figure 20a).

Stage 2. The Syria Planum highlands were created by magmatic emplacement and volcanic eruptions. This caused the eastward emplacement of lava flows against the Thaumasia highlands in the east (Figure 20b).

Stage 3. Continued east–west crustal shortening created the wrinkle ridges. The formation of the wrinkle ridges may have occurred when some of the lavas were still warm and viscous, creating the flow-front-like ridge morphology (Figure 20c).

Stage 4. Regional glaciation moved an overlying ice sheet atop the wrinkle ridges. This process deposited regionally extensive boulders, created striated surfaces, and formed eskers at the base of the ice sheet (Figure 20d).

Stage 5. Deglaciation and the deposition of locally highly concentrated glacial flours created mantled and un-mantled terrains (Figure 20e).

Following are the most important implications of our proposed model:

(1) The Tharsis rise region experienced volcanism first, followed by tectonic compression, which in turn was followed by glaciation. This sequence of events differs significantly from those inferred earlier (e.g., Cassanelli and Head, 2019).

(2) The morphology of the wrinkle ridges in the study area may have been modified by both glacial deposition and erosion, not to mention the later effect of wind erosion. This inference casts uncertainties on using the present-day wrinkle-ridge morphology to deduce the subsurface geometry of the thrusts below the fold-generated ridges. Erosion modification of the original wrinkle-ridge morphology means that the topographic profiles can offer only minimum values of shortening when the profile lines are straightened, and the true shortening strain could be much greater. A potential way of overcoming this issue in the future may be to use ground-penetrating radar capable of imaging folded layers below the ridges.

(3) A key implication of our model is that folding and lava emplacement may have occurred synchronously, as discussed in Watters (1988). The folding of warm and ductile lava beds helps explain the flow-front-like morphology associated with the margins of some wrinkle ridges. Coeval shortening and volcanism during the construction of the Tharsis rise were predicted in the slab rollback model of Yin A (2012b).

Despite the fact that our proposed landscape model provides a self-consistent explanation for the evolution of the central and eastern Tharsis region, the model is not unique, and as a note of caution, all competing mechanisms for generating wrinkle ridges, boulder deposits, boulder-bearing ridges, and mantled terrains remain viable. Differentiating these competing hypotheses will require more systematic investigations of wrinkle ridges in other geologic settings on Mars and other rocky bodies in the inner solar system. For example, we cannot completely rule out impact gardening and autobrecciation as boulder-generating mechanisms in the study area. Similarly, the boulder-bearing curvilinear ridges could have been formed by open-water fluvial processes if the current landscape has been altered since ridge formation.

6. Conclusions

Geological mapping, topographic-data analysis, and the examination of high-resolution satellite images at resolutions of 25–50 cm /pixel to 6 m/pixel allowed us to test a suite of models for the formation of wrinkle ridges in the central Tharsis region. The main results of this work are in the form of (1) a regional geomorphological map prepared by using a CTX mosaic at a resolution of 6 m /pixel and (2) a local geomorphologic map prepared by using a HiRISE image at a resolution of 50 cm/pixel. Our work, when viewed in the context of existing research, suggests the following sequence of events for the landscape evolution of the central Tharsis region: (1) the creation of a plateau region along the eastern margin of the Tharsis rise by east-directed, crustal-scale thrusting; (2) the coeval formation of a volcanic plateau that acted as the source of east-flowing lavas that filled a basin between the tectonically induced plateau in the east and the volcanically generated plateau in the west; (3) continued east–west crustal shortening during the emplacement of the lava flows that favored the formation of wrinkle ridges because of thermal weakening of the uppermost crust; (4) regional glaciation postdating lava emplacement that produced extensive boulder-bearing materials, striated surfaces, and glacial eskers that are superposed on the earlier formed wrinkle ridges; and (5) the deposition of locally highly concentrated glacial flours laid down during deglaciation that selectively mantled the tectonically deformed and glacially modified landscape. Our work supports the early suggestion that the Tharsis wrinkle ridges were created by horizontal shortening induced by crustal-scale tectonic processes. However, the occurrence of flow-front-like margins of many mapped wrinkle ridges suggests that the deformation was ductile, at least locally, most likely when the uppermost crust was still hot and weak. Glacial modification of the earlier formed wrinkle ridges means that the present-day wrinkle-ridge morphologies should not be used to invert the geometry of the blind thrust systems below.

Acknowledgments

We thank the National Aeronautics and Space Administration (NASA) for making the CTX and HiRISE images available and the HiRISE team at the University of Arizona for providing the HiView software used for analyzing the HiRISE images. We also thank the European Space Agency for making their HRSC DEM data available for this study. This research could not have been performed without the freely available JMARS software. Feedback on the work from University of California, Los Angeles (UCLA) colleagues Dave Paige, Mackenzie Day, and Seulgi Moon helped improved the original manuscript. Three journal reviewers provided careful, critical, and constructive comments that led to a significant improvement of the original draft. The work presented in this paper is the result of curiosity-driven research and was not supported by any funding agencies.

References

Agard, P., Omrani, J., Jolivet, L., Whitechurch, H., Vrielynck, B., Spakman, W., Monié, P., Meyer, B., and Wortel, R. (2011). Zagros orogeny: A subduction-dominated process. *Geol. Mag.*, *148*(5–6), 692–725. https://doi.org/10.1017/S001675681100046X

Allemand, P., and Thomas, P. G. (1995). Localization of Martian ridges by impact craters: Mechanical and chronological implications. *J. Geophys. Res.*: *Planets*, *100*(E2), 3251–3262. https://doi.org/10.1029/94JE03081

Anderson, M. P. (1989). Hydrogeologic facies models to delineate large-scale spatial trends in glacial and glaciofluvial sediments. *Geological Society of America Bulletin*, *101*(4), 501–511.

Andrews-Hanna, J. C. (2020). The tectonic architecture of wrinkle ridges on Mars. *Icarus*, *351*, 113937. https://doi.org/10.1016/j.icarus.2020.113937

Ansan, V., and Mangold, N. (2006). New observations of Warrego Valles, Mars: Evidence for precipitation and surface runoff. *Planet. Space Sci.*, *54*(3), 219–242. https://doi.org/10.1016/j.pss.2005.12.009

Ansan, V., and Mangold, N. (2013). 3D morphometry of valley networks on Mars from HRSC/MEX DEMs: Implications for climatic evolution through time. *J. Geophys. Res.*: *Planets*, *118*(9), 1873–1894. https://doi.org/10.1002/jgre.20117

Atkins, C. B. (2013). Geomorphological evidence of cold-based glacier activity in South Victoria Land, Antarctica. *Geol. Soc. Lond. Spec. Publ.*, *381*(1), 299–318.

https://doi.org/10.1144/SP381.18

Baker, V. R., Maruyama, S., and Dohm, J. M. (2007). Tharsis superplume and the geological evolution of early Mars. In D. A. Yuen et al. (Eds.), *Superplumes: Beyond Plate Tectonics* (pp. 507–522). Dordrecht: Springer. https://doi.org/10.1007/978-1-4020-5750-2_16

Baldwin, R. B. (1968). Lunar mascons: Another interpretation. *Science*, *162*(3860), 1407–1408. https://doi.org/10.1126/science.162.3860.1407

Bally, A. W., Gordy, P. L., and Stewart, G. A. (1966). Structure, seismic data, and orogenic evolution of southern Canadian Rocky Mountains. *Bull. Can. Petrol. Geol.*, *14*(3), 337–381. https://doi.org/10.35767/gscpgbull.14.3.337

Banerdt, W.B., Golombek, M.P., and Tanaka, K.L., 1992. Stress and tectonics on Mars. In: H. H. Kieffer et al. (Eds.), *Mars*. Univ. of Arizona Press, Tucson, 249–297.

Baptista, A. R., Mangold, N., Ansan, V., Baratoux, D., Lognonné, P., Alves, E. I., Williams, D. A., Bleacher, J. E., Masson, P., and Neukum, G. (2008). A swarm of small shield volcanoes on Syria Planum, Mars. *J. Geophys. Res.: Planets*, *113*(E9), E09010. https://doi.org/10.1029/2007JE002945

Basilevsky, A. T., and Head, J. W. (2006). Impact craters on regional plains on Venus: Age relations with wrinkle ridges and implications for the geological evolution of Venus. *J. Geophys. Res.: Planets*, *111*(E3), E03006. https://doi.org/10.1029/2005JE002473

Benn, D. I., Bolch, T., Hands, K., Gulley, J., Luckman, A., Nicholson, L. I., Quincey, D., Thompson, S., Toumi, R., and Wiseman, S. (2012). Response of debris-covered glaciers in the Mount Everest region to recent warming, and implications for outburst flood hazards. *Earth-Sci. Rev.*, *114*(1–2), 156–174. https://doi.org/10.1016/j.earscirev.2012.03.008

Berman, D. C., Balme, M. R., Rafkin, S. C. R., and Zimbelman, J. R. (2011). Transverse aeolian ridges (TARs) on Mars II: Distributions, orientations, and ages. *Icarus*, *213*(1), 116–130. https://doi.org/10.1016/j.icarus.2011.02.014

Bethell, E. M., Ernst, R. E., and Samson, C. (2022). Analysis of Venusian wrinkle ridge morphometry using stereo-derived topography: A case study from southern Eistla Regio. *J. Geophys. Res.: Planets*, *127*(5), e2021JE006879. https://doi.org/10.1029/2021JE006879

Bilotti, F., and Suppe, J. (1999). The global distribution of wrinkle ridges on Venus. *Icarus*, *139*(1), 137–157. https://doi.org/10.1006/icar.1999.6092

Borgia, A. (1994). Dynamic basis of volcanic spreading. *J. Geophys. Res.: Solid Earth*, *99*(B9), 17791–17804. https://doi.org/10.1029/94JB00578

Bouley, S., Baratoux, D., Paulien, N., Missenard, Y., and Saint-Bézar, B. (2018). The revised tectonic history of Tharsis. *Earth Planet. Sci. Lett.*, *488*, 126–133. https://doi.org/10.1016/j.epsl.2018.02.019

Boulton, G. S. (1978). Boulder shapes and grain-size distributions of debris as indicators of transport paths through a glacier and till genesis. *Sedimentology*, *25*(6), 773–799. https://doi.org/10.1111/j.1365-3091.1978.tb00329.x

Bridges, N. T., Banks, M. E., Beyer, R. A., Chuang, F. C., Noe Dobrea, E. Z., Herkenhoff, K. E., Keszthelyi, L. P., Fishbaugh, K. E., McEwen, A. S., … Wray, J. J. (2010). Aeolian bedforms, yardangs, and indurated surfaces in the Tharsis Montes as seen by the HiRISE camera: Evidence for dust aggregates. *Icarus*, *205*(1), 165–182. https://doi.org/10.1016/j.icarus.2009.05.017

Brodzikowski, K., and Van Loon, A. J. (1987). A systematic classification of glacial and periglacial environments, facies and deposits. *Earth-Science Reviews*, *24*(5), 297–381.

Brunetti, M. T., Guzzetti, F., Cardinali, M., Fiorucci, F., Santangelo, M., Mancinelli, P., Komatsu, G., and Borselli, L. (2014). Analysis of a new geomorphological inventory of landslides in Valles Marineris, Mars. *Earth Planet. Sci. Lett.*, *405*, 156–168. https://doi.org/10.1016/j.epsl.2014.08.025

Bryan, W. B. (1973). Wrinkle-ridges as deformed surface crust on ponded mare lava. *Lunar and Planetary Science Conference Proceedings*, *4*, 93–106.

Butcher, F. E. G., Balme, M. R., Conway, S. J., Gallagher, C., Arnold, N. S., Storrar, R. D., Lewis, S. R., Hagermann, A., and Davis, J. M. (2021). Sinuous ridges in Chukhung crater, Tempe Terra, Mars: Implications for fluvial, glacial, and glaciofluvial activity. *Icarus*, *357*, 114131. https://doi.org/10.1016/j.icarus.2020.114131

Butcher, F. E., Balme, M. R., Gallagher, C., Arnold, N. S., Conway, S. J., Hagermann, A., and Lewis, S. R. (2017). Recent basal melting of a mid-latitude glacier on Mars. *Journal of Geophysical Research*: *Planets*, *122*(12), 2445–246.

Butcher, F. E., Conway, S. J., and Arnold, N. S. (2016). Are the dorsa argentea on mars eskers?. *Icarus*, *275*, 65–84.

Byrne, P. K., Klimczak, C., Celâl Şengör, A. M., Solomon, S. C., Watters, T. R., and Hauck, S. A., II. (2014). Mercury's global contraction much greater than earlier estimates. *Nat. Geosci.*, *7*(4), 301–307. https://doi.org/10.1038/ngeo2097

Byrne, P. K., Ghail, R. C., Şengör, A. M. C., James, P. B., Klimczak, C., and Solomon, S. C. (2021). A globally fragmented and mobile lithosphere on Venus. *Proc. Natl. Acad. Sci. USA*, *118*(26), e2025919118. https://doi.org/10.1073/pnas.2025919118

Carr, M. H. (1973). Volcanism on Mars. *J. Geophys. Res.*, *78*(20), 4049–4062. https://doi.org/10.1029/JB078i020p04049

Carr, M. H. (1974). Tectonism and volcanism of the Tharsis region of Mars. *J. Geophys. Res.*, *79*(26), 3943–3949. https://doi.org/10.1029/JB079i026p03943

Carr, M. H., Greeley, R., Blasius, K. R., Guest, J. E., and Murray, J. B. (1977). Some Martian volcanic features as viewed from the Viking orbiters. *J. Geophys. Res.*, *82*(28), 3985–4015. https://doi.org/10.1029/JS082i028p03985

Carr, M. H., and Head, J. W., III. (2010). Geologic history of Mars. *Earth Planet. Sci. Lett.*, *294*(3–4), 185–203. https://doi.org/10.1016/j.epsl.2009.06.042

Cassanelli, J. P., and Head, J. W. (2019). Glaciovolcanism in the Tharsis volcanic province of Mars: Implications for regional geology and hydrology. *Planet. Space Sci.*, *169*, 45–69. https://doi.org/10.1016/j.pss.2019.02.006

Chen, H. Z., and Yin, A. (2022). Impacts of thrusting, extensional faulting, and glaciation on cratering records of Pluto's largest moon Charon: Implications for the evolution of Kuiper belt objects. *Earth Planet. Phys.*, *6*(6), 495–521. https://doi.org/10.26464/epp2022049

Christensen, P. R., Engle, E., Anwar, S., Dickenshied, S., Noss, D., Gorelick, N., and Weiss-Malik, M. (2009). JMARS—A planetary GIS. In *AGU Fall Meeting Abstracts*. Washington, DC: American Geophysical Union.

Clark, P. U., and Walder, J. S. (1994). Subglacial drainage, eskers, and deforming beds beneath the Laurentide and Eurasian ice sheets. *Geol. Soc. Am. Bull.*, *106*(2), 304–314. https://doi.org/10.1130/0016-7606(1994)106<0304:SDEADB>2.3.CO;2

Cole, H. M., and Andrews-Hanna, J. C. (2017). The anatomy of a wrinkle ridge revealed in the wall of Melas Chasma, Mars. *J. Geophys. Res.: Planets*, *122*(5), 889–900. https://doi.org/10.1002/2017JE005274

Crane, K. T., and Klimczak, C. (2019). Tectonic patterns of shortening landforms in Mercury's northern smooth plains. *Icarus*, *317*, 66–80. https://doi.org/10.1016/j.icarus.2018.05.034

Dębniak, K., Mège, D., and Gurgurewicz, J. (2017). Geomorphology of Ius Chasma, Valles Marineris, Mars. *J. Maps*, *13*(2), 260–269. https://doi.org/10.1080/17445647.2017.1296790

De Hon, R. A. (1982). Martian volcanic materials: Preliminary thickness estimates in the eastern Tharsis region. *J. Geophys. Res.: Solid Earth*, *87*(B12), 9821–9828. https://doi.org/10.1029/JB087iB12p09821

Denlinger, R. P., and Morgan, J. K. (2014). Instability of Hawaiian volcanoes. In M. P. Poland et al. (Eds.), *Characteristics of Hawaiian Volcanoes* (pp. 149–176). Reston, VA: U.S. Geological Survey. https://doi.org/10.3133/pp18014

Dickson, J. L., Kerber, L. A., Fassett, C. I., and Ehlmann, B. L. (2018). A global, blended CTX mosaic of Mars with vectorized seam mapping: A new mosaicking pipeline using principles of non-destructive image editing. In *Proceedings of the 49th Annual Lunar and Planetary Science Conference* (pp. 1–2). The Woodlands, TX, USA.

Dohm, J. M., and Tanaka, K. L. (1999). Geology of the Thaumasia region, Mars: Plateau development, valley origins, and magmatic evolution. *Planet. Space Sci.*, *47*(3–4), 411–431. https://doi.org/10.1016/S0032-0633(98)00141-X

Dohm, J. M., Baker, V. R., Maruyama, S., and Anderson, R. C. (2007). Traits and evolution of the Tharsis superplume, Mars. In D. A. Yuen et al. (Eds.), *Superplumes: Beyond Plate Tectonics* (pp. 523–536). Dordrecht, Netherlands: Springer. https://doi.org/10.1007/978-1-4020-5750-2_17

Dohm, J. M., Maruyama, S., Kido, M., and Baker, V. R. (2018). A possible anorthositic continent of early Mars and the role of planetary size for the inception of Earth-like life. *Geosci. Front.*, *9*(4), 1085–1098. https://doi.org/10.1016/j.gsf.2016.12.003

Edgett, K. S. (1997). Aeolian dunes as evidence for explosive volcanism in the Tharsis region of Mars. *Icarus*, *130*(1), 96–114. https://doi.org/10.1006/icar.1997.5806

Edwards, C. S., Nowicki, K. J., Christensen, P. R., Hill, J., Gorelick, N., and Murray, K.

(2011). Mosaicking of global planetary image datasets: 1. Techniques and data processing for Thermal Emission Imaging System (THEMIS) multi-spectral data. *J. Geophys. Res.*: *Planets*, *116*(E10), E10008. https://doi.org/10.1029/2010JE003755

Elger, T. G. (1895). *The Moon: A Full Description and Map of Its Principal Physical Features*. London: George Philip & Son.

Evans, D. J. A. (2003). *Glacial Landsystems*. London: Hodder Arnold.

Fergason, R. L, Hare, T. M., and Laura, J. (2018). HRSC and MOLA Blended Digital Elevation Model at 200 m v2, Astrogeology PDS Annex, U. S. Geological Survey. http://bit.ly/HRSC_MOLA_Blend_v0.

Fielder, G. (1961). *Structure of the Moon's Surface*. New York: Pergamon Press.

Fielder, G., and Kiang, T. (1962). The segmental structure of wrinkle ridges and the lunar grid system. *The Observatory*, *82*, 8–9.

Fielder, G. (1965). *Lunar Geology*. Chester Springs, PA: Dufour Editions.

Freed, A. M., Melosh, H. J., and Solomon, S. C. (2001). Tectonics of mascon loading: Resolution of the strike-slip faulting paradox. *J. Geophys. Res.*: *Planets*, *106*(E9), 20603–20620. https://doi.org/10.1029/2000JE001347

Fueten, F., Flahaut, J., Le Deit, L., Stesky, R., Hauber, E., and Gwinner, K. (2011). Interior layered deposits within a perched basin, southern Coprates Chasma, Mars: Evidence for their formation, alteration, and erosion. *J. Geophys. Res.*: *Planets*, *116*(E2), E02003. https://doi.org/10.1029/2010JE003695

Gallagher, C., and Balme, M. (2015). Eskers in a complete, wet-based glacial system in the Phlegra Montes region, Mars. *Earth Planet. Sci. Lett.*, *431*, 96–109. https://doi.org/10.1016/j.epsl.2015.09.023

Golabek, G. J., Keller, T., Gerya, T. V., Zhu, G. Z., Tackley, P. J., and Connolly, J. A. D. (2011). Origin of the Martian dichotomy and Tharsis from a giant impact causing massive magmatism. *Icarus*, *215*(1), 346–357. https://doi.org/10.1016/j.icarus.2011.06.012

Golombek, M. P., Plescia, J. B., and Franklin, B. J. (1991). Faulting and folding in the formation of planetary wrinkle ridges. *Planetary Science Conference Proceedings*, *21*, 679–693.

Golombek, M. P., Anderson, F. S., and Zuber, M. T. (2001). Martian wrinkle ridge topography: Evidence for subsurface faults from MOLA. *J. Geophys. Res.*: *Planets*, *106*(E10), 23811–23821. https://doi.org/10.1029/2000JE001308

Golombek, M. P., and Phillips, R. J. (2010). Mars tectonics. In T. R. Watters et al. (Eds.), *Planetary Tectonics* (pp. 183–232). Cambridge: Cambridge University Press. https://doi.org/10.1017/CBO9780511691645.006

Gourronc, M., Bourgeois, O., Mège, D., Pochat, S., Bultel, B., Massé, M., Le Deit, L., Le Mouélic, S., and Mercier, D. (2014). One million cubic kilometers of fossil ice in Valles Marineris: Relicts of a 3.5 Gy old glacial landsystem along the Martian equator. *Geomorphology*, *204*, 235–255. https://doi.org/10.1016/j.geomorph.2013.08.009

Grant, J. A., Irwin, R. P., III, Grotzinger, J. P., Milliken, R. E., Tornabene, L. L., McEwen, A. S., Weitz, C. M., Squyres, S. W., Glotch, T. D., and Thomson, B. J. (2008). HiRISE imaging of impact megabreccia and sub-meter aqueous strata in Holden Crater, Mars. *Geology*, *36*(3), 195–198. https://doi.org/10.1130/G24340A.1

Grau Galofre, A., Jellinek, A. M., and Osinski, G. R. (2020). Valley formation on early Mars by subglacial and fluvial erosion. *Nat. Geosci.*, *13*(10), 663–668. https://doi.org/10.1038/s41561-020-0618-x

Greeley, R., and Spudis, P. D. (1978a). Volcanism in the cratered terrain hemisphere of Mars. *Geophys. Res. Lett.*, *5*(6), 453–455. https://doi.org/10.1029/GL005i006p00453

Greeley, R., and Spudis, P. D. (1978b). Ridges in Western Columbia Plateau, Washington—Analogs to mare-type ridges?. In *Lunar and Planetary Science Conference* (Vol. 9, 411).

Guest, J. E., and Fielder, G. (1968). Lunar ring structures and the nature of the Maria. *Planet. Space Sci.*, *16*(5), 665–673. https://doi.org/10.1016/0032-0633(68)90105-0

Guest, J. E. (1971). Geology of the farside crater Tsiolkovsky. In G. Fielder (Ed.), *Geology and Physics of the Moon* (pp. 93–103). Amsterdam: Elsevier.

Hansen, V. L., and Olive, A. (2010). Artemis, Venus: The largest tectonomagmatic feature in the solar system? *Geology*, *38*(5), 467–470. https://doi.org/10.1130/G30643.1

Harder, H., and Christensen, U. R. (1996). A one-plume model of Martian mantle convection. *Nature*, *380*(6574), 507–509. https://doi.org/10.1038/380507a0

Hartmann, W. K., Anguita, J., de la Casa, M. A., Berman, D. C., and Ryan, E. V. (2001). Martian cratering 7: The role of impact gardening. *Icarus*, *149*(1), 37–53. https://doi.org/10.1006/icar.2000.6532

Hauber, E., Bleacher, J., Gwinner, K., Williams, D., and Greeley, R. (2009). The topography and morphology of low shields and associated landforms of plains volcanism in the Tharsis region of Mars. *J. Volcanol. Geoth. Res.*, *185*(1–2), 69–95. https://doi.org/10.1016/j.jvolgeores.2009.04.015

Head, J. W., III, Kreslavsky, M. A., and Pratt, S. (2002). Northern lowlands of Mars: Evidence for widespread volcanic flooding and tectonic deformation in the Hesperian Period. *J. Geophys. Res.: Planets*, *107*(E1), 3-1–3-29. https://doi.org/10.1029/2000JE001445

Head, J. W., Marchant, D. R., Dickson, J. L., Kress, A. M., and Baker, D. M. (2010). Northern mid-latitude glaciation in the Late Amazonian period of Mars: Criteria for the recognition of debris-covered glacier and valley glacier landsystem deposits. *Earth Planet. Sci. Lett.*, *294*(3–4), 306–320. https://doi.org/10.1016/j.epsl.2009.06.041

Hicock, S. R. (1991). On subglacial stone pavements in till. *J. Geol.*, *99*(4), 607–619. https://doi.org/10.1086/629520

Howard, K. A., and Muehlberger, W. R. (1973). Mare ridges and related studies: Part C: Lunar thrust faults in the Taurus–Littrow region. Washington, DC: National Aeronautics and Space Administration.

Ivanov, M. A., and Head, J. W. (2011). Global geological map of Venus. *Planet. Space Sci.*, *59*(13), 1559–1600. https://doi.org/10.1016/j.pss.2011.07.008

Jordan, T. E., Isacks, B. L., Allmendinger, R. W., Brewer, J. A., Ramos, V. A., and Ando, C. J. (1983). Andean tectonics related to geometry of subducted Nazca plate. *Geol. Soc. Am. Bull.*, *94*(3), 341–361. https://doi.org/10.1130/0016-7606(1983)94<341:ATRTGO>2.0.CO;2

Kakaria, R., and Yin, A. (2023). Subglacial catastrophic-flood origin of linear and curvilinear flat-rimmed pit chains on Mars: Evidence from geomorphological mapping and detailed landform analysis. *Icarus*, in press. https://doi.org/10.1016/j.icarus.2023.115439

Karagoz, O., Kenkmann, T., and Wulf, G. (2022a). Insights into the subsurface structure of wrinkle ridges on Mars. *Earth Planet. Sci. Lett.*, *595*, 117759. https://doi.org/10.1016/j.epsl.2022.117759

Karagoz, O., Kenkmann, T., and Wulf, G. (2022b). Circum-Tharsis wrinkle ridges at Lunae Planum: Morphometry, formation, and crustal implications. *Icarus*, *374*, 114808. https://doi.org/10.1016/j.icarus.2021.114808

Kargel, J. S., and Strom, R. G. (1992). Ancient glaciation on Mars. *Geology*, *20*(1), 3–7. https://doi.org/10.1130/0091-7613(1992)020<0003:AGOM>2.3.CO;2

Kreslavsky, M. A., and Basilevsky, A. T. (1998). Morphometry of wrinkle ridges on Venus: Comparison with other planets. *J. Geophys. Res.: Planets*, *103*(E5), 11103–11111. https://doi.org/10.1029/98JE00360

Li, B., Ling, Z. C., Zhang, J., Chen, J., Ni, Y. H., and Liu, C. L. (2018). Displacement-length ratios and contractional strains of lunar wrinkle ridges in Mare Serenitatis and Mare Tranquillitatis. *J. Struct. Geol.*, *109*, 27–37. https://doi.org/10.1016/j.jsg.2018.01.003

Lillis, R. J., Dufek, J., Bleacher, J. E., and Manga, M. (2009). Demagnetization of crust by magmatic intrusion near the Arsia Mons volcano: Magnetic and thermal implications for the development of the Tharsis province, Mars. *J. Volcanol. Geoth. Res.*, *185*(1–2), 123–138. https://doi.org/10.1016/j.jvolgeores.2008.12.007

Lucchitta, B. K. (1978). Morphology of chasma walls, Mars. *J. Res. US Geol. Surv.*, *6*(5), 651–662.

Lucchitta, B. K., and Klockenbrink, J. L. (1981). Ridges and scarps in the equatorial belt of Mars. *Moon Planets*, *24*(4), 415–429. https://doi.org/10.1007/BF00896907

Malin, M. C., Bell, J. F., Cantor, B. A., Caplinger, M. A., Calvin, W. M., Clancy, R. T., Edgett, K. S., Edwards, L., Haberle, R. M., … Wolff, M. J. (2007). Context camera investigation on board the Mars Reconnaissance Orbiter. *J. Geophys. Res.: Planets*, *112*(E5), E05S04. https://doi.org/10.1029/2006JE002808

Mangold, N., Allemand, P., and Thomas, P. G. (1998). Wrinkle ridges of Mars: Structural analysis and evidence for shallow deformation controlled by ice-rich décollements. *Planet. Space Sci.*, *46*(4), 345–356. https://doi.org/10.1016/S0032-0633(97)00195-5

Mangold, N., Ansan, V., Masson, P., Quantin, C., and Neukum, G. (2008). Geomorphic study of fluvial landforms on the northern Valles Marineris plateau, Mars. *J. Geophys. Res.: Planets*, *113*(E8), E08009. https://doi.org/

10.1029/2007JE002985

Mangold, N., Loizeau, D., Poulet, F., Ansan, V., Baratoux, D., LeMouelic, S., Bardintzeff, J. M., Platevoet, B., Toplis, M., … Neukum, G. (2010). Mineralogy of recent volcanic plains in the Tharsis region, Mars, and implications for platy-ridged flow composition. *Earth Planet. Sci. Lett.*, *294*(3–4), 440–450. https://doi.org/10.1016/j.epsl.2009.07.036

Maxwell, T. A., El-Baz, F., and Ward, S. H. (1975). Distribution, morphology, and origin of ridges and arches in Mare Serenitatis. *Geol. Soc. Am. Bull.*, *86*(9), 1273–1278. https://doi.org/10.1130/0016-7606(1975)86<1273:DMAOOR>2.0.CO;2

Maxwell, T. A., and Gifford, A. W. (1980). Ridge systems of Caloris: Comparison with lunar basins. In *Lunar and Planetary Science Conference Proceedings* (pp. 2447–2462). Houston, TX, United States.

McGill, G. E. (1993). Wrinkle ridges, stress domains, and kinematics of Venusian plains. *Geophys. Res. Lett.*, *20*(21), 2407–2410. https://doi.org/10.1029/93GL02635

McGill, G. E. (2004). Tectonic and stratigraphic implications of the relative ages of Venusian plains and wrinkle ridges. *Icarus*, *172*(2), 603–612. https://doi.org/10.1016/j.icarus.2004.07.008

McQuarrie, N., Horton, B. K., Zandt, G., Beck, S., and DeCelles, P. G. (2005). Lithospheric evolution of the Andean fold–thrust belt, Bolivia, and the origin of the central Andean plateau. *Tectonophysics*, *399*(1–4), 15–37. https://doi.org/10.1016/j.tecto.2004.12.013

Mège, D., and Masson, P. (1996a). A plume tectonics model for the Tharsis province, Mars. *Planet. Space Sci.*, *44*(12), 1499–1546. https://doi.org/10.1016/S0032-0633(96)00113-4

Mège, D., and Masson, P. (1996b). Stress models for Tharsis formation, Mars. *Planet. Space Sci.*, *44*(12), 1471–1497. https://doi.org/10.1016/S0032-0633(96)00112-2

Mège, D., and Reidel, S. P. (2001). A method for estimating 2D wrinkle ridge strain from application of fault displacement scaling to the Yakima folds, Washington. *Geophys. Res. Lett.*, *28*(18), 3545–3548. https://doi.org/10.1029/2001GL012934

Mège, D., and Bourgeois, O. (2011). Equatorial glaciations on Mars revealed by gravitational collapse of Valles Marineris wallslopes. *Earth Planet. Sci. Lett.*, *310*(3–4), 182–191. https://doi.org/10.1016/j.epsl.2011.08.030

Montési, L. G. J., and Zuber, M. T. (2003). Clues to the lithospheric structure of Mars from wrinkle ridge sets and localization instability. *J. Geophys. Res.: Planets*, *108*(E6), 5048. https://doi.org/10.1029/2002JE001974

Montgomery, D. R., Som, S. M., Jackson, M. P. A., Schreiber, B. C., Gillespie, A. R., and Adams, J. B. (2009). Continental-scale salt tectonics on Mars and the origin of Valles Marineris and associated outflow channels. *GSA Bull.*, *121*(1–2), 117–133. https://doi.org/10.1130/B26307.1

Morgan, J. K., Moore, G. F., Hills, D. J., and Leslie, S. (2000). Overthrusting and sediment accretion along Kilauea's mobile south flank, Hawaii: Evidence for volcanic spreading from marine seismic reflection data. *Geology*, *28*(7), 667–670. https://doi.org/10.1130/0091-7613(2000)28<667:OASAAK>2.0.CO;2

Mouginis-Mark, P. J. (1987). Water or ice in the Martian regolith? Clues from rampart craters seen at very high resolution. *Icarus*, *71*(2), 268–286. https://doi.org/10.1016/0019-1035(87)90152-7

Mouginis-Mark, P. J., and Wilson, L. (2019). Late-stage intrusive activity at Olympus Mons, Mars: Summit inflation and giant dike formation. *Icarus*, *319*, 459–469. https://doi.org/10.1016/j.icarus.2018.09.038

Mouginis-Mark, P. J., Wilson, L., and Head III, J. W. (1982). Explosive volcanism on Hecates Tholus, Mars: Investigation of eruption conditions. *Journal of Geophysical Research*: *Solid Earth*, *87*(B12), 9890–9904.

Mouginis-Mark, P. J., Zimbelman, J. R., Crown, D. A., Wilson, L., and Gregg, T. K. P. (2022). Martian volcanism: Current state of knowledge and known unknowns. *Geochemistry*, *82*(4), 125886. https://doi.org/10.1016/J.CHEMER.2022.125886

Mueller, K., and Golombek, M. (2004). Compressional structures on Mars. *Annu. Rev. Earth Planet. Sci.*, *32*, 435–464. https://doi.org/10.1146/annurev.earth.32.101802.120553

Murchie, S. L., Watters, T. R., Robinson, M. S., Head, J. W., Strom, R. G., Chapman, C. R., Solomon, S. C., McClintock, W. E., Prockter, L. M., ... Blewett, D. T. (2008). Geology of the Caloris basin, Mercury: A view from MESSENGER. *Science*, *321*(5885), 73–76. https://doi.org/10.1126/science.1159261

Murray, B. C., Belton, M. J. S., Danielson, G. E., Davies, M. E., Gault, D., Hapke, B., O'Leary, B., Strom, R. G., Suomi, V., and Trask, N. (1974). Mariner 10 pictures of Mercury: First results. *Science*, *184*(4135), 459–461. https://doi.org/10.1126/science.184.4135.459

Nahm, A. L., and Schultz, R. A. (2011). Magnitude of global contraction on Mars from analysis of surface faults: Implications for Martian thermal history. *Icarus*, *211*(1), 389–400. https://doi.org/10.1016/j.icarus.2010.11.003

Neukum, G., Jaumann, R., Hoffmann, H., Hauber, E., Head, J. W., Basilevsky, A. T., Ivanov, B. A., Werner, S. C., van Gasselt, S., … The HRSC Co-Investigator Team. (2004). Recent and episodic volcanic and glacial activity on Mars revealed by the High Resolution Stereo Camera. *Nature*, *432*(7020), 971–979. https://doi.org/10.1038/nature03231

Nimmo, F., and Tanaka, K. (2005). Early crustal evolution of Mars. *Annu. Rev. Earth Planet. Sci.*, *33*, 133–161.

Okubo, C. H., and Schultz, R. A. (2004). Mechanical stratigraphy in the western equatorial region of Mars based on thrust fault–related fold topography and implications for near-surface volatile reservoirs. *Geol. Soc. Am. Bull.*, *116*(5–6), 594–605. https://doi.org/10.1130/B25361.1

Orr, T. R., Bleacher, J. E., Patrick, M. R., and Wooten, K. M. (2015). A sinuous tumulus over an active lava tube at Kīlauea Volcano: Evolution, analogs, and hazard forecasts. *Journal of Volcanology and Geothermal Research*, *291*, 35–48.

Parsons, W. H. (1969). Criteria for the recognition of volcanic breccias. *Geological Society of America Memoir*, *115*, 263–304.

Phillips, R. J., and Lambeck, K. (1980). Gravity fields of the terrestrial planets: Long-wavelength anomalies and tectonics. *Rev. Geophys.*, *18*(1), 27–76. https://doi.org/10.1029/RG018i001p00027

Phillips, R. J., Conel, J. E., Abbott, E. A., Sjogren, W. L., and Morton, J. B. (1972). Mascons: Progress toward a unique solution for mass distribution. *Journal of Geophysical Research*, *77*(35), 7106–7114.

Phillips, R. J., Zuber, M. T., Solomon, S. C., Golombek, M. P., Jakosky, B. M., Banerdt, W. B., Smith, D. E., Williams, R. M. E., Hynek, B. M., ... Hauck, S. A., II. (2001). Ancient geodynamics and global-scale hydrology on Mars. *Science*, *291*(5513), 2587–2591. https://doi.org/10.1126/science.1058701

Plescia, J. B., and Golombek, M. P. (1986). Origin of planetary wrinkle ridges based on the study of terrestrial analogs. *Geol. Soc. Am. Bull.*, *97*(11), 1289–1299. https://doi.org/10.1130/0016-7606(1986)97<1289:OOPWRB>2.0.CO;2

Price, R. A. (1981). The Cordilleran foreland thrust and fold belt in the southern Canadian Rocky Mountains. *Geol. Soc. Lond. Spec. Publ.*, *9*(1), 427–448. https://doi.org/10.1144/gsl.sp.1981.009.01.39

Rahn, P. H. (1971). Lunar wrinkle ridges indicative of strike-slip faulting: Discussion. *Geol. Soc. Am. Bull.*, *82*(8), 2365–2366. https://doi.org/10.1130/0016-7606(1971)82[2365:LWRIOS]2.0.CO;2

Reese, C. C., Solomatov, V. S., Baumgardner, J. R., Stegman, D. R., and Vezolainen, A. V. (2004). Magmatic evolution of impact-induced Martian mantle plumes and the origin of Tharsis. *J. Geophys. Res.: Planets*, *109*(E8), E08009. https://doi.org/10.1029/2003JE002222

Reidel, S. P. (1984). The Saddle Mountains: The evolution of an anticline in the Yakima fold belt. *Am. J. Sci.*, *284*(8), 942–978. https://doi.org/10.2475/ajs.284.8.942

Richardson, J. A., Bleacher, J. E., and Glaze, L. S. (2013). The volcanic history of Syria Planum, Mars. *J. Volcanol. Geoth. Res.*, *252*, 1–13. https://doi.org/10.1016/j.jvolgeores.2012.11.007

Richardson, J. A., Bleacher, J. E., Connor, C. B., and Glaze, L. S. (2021). Small volcanic vents of the Tharsis Volcanic Province, Mars. *J. Geophys. Res.: Planets*, *126*(2), e2020JE006620. https://doi.org/10.1029/2020JE006620

Ruj, T., and Kawai, K. (2021). A global investigation of wrinkle ridge formation events; implications towards the thermal evolution of Mars. *Icarus*, *369*, 114625. https://doi.org/10.1016/j.icarus.2021.114625

Schleicher, L. S., Watters, T. R., Martin, A. J., and Banks, M. E. (2019). Wrinkle ridges on Mercury and the Moon within and outside of Mascons. *Icarus*, *331*, 226–237. https://doi.org/10.1016/j.icarus.2019.04.013

Schubert, G., Solomon, S. C., Turcotte, D. L., Drake, M. J., and Sleep, N. H. (1992). Origin and thermal evolution of Mars. In H. H. Kieffer et al. (Eds.), *Mars* (pp. 147–183). Tucson: University of Arizona Press.

Schultz, R. A. (2000). Localization of bedding plane slip and backthrust faults above blind thrust faults: Keys to wrinkle ridge structure. *J. Geophys. Res.: Planets*, *105*(E5), 12035–12052. https://doi.org/10.1029/1999JE001212

Scott, E., and Wilson, L. (2003). Did the Alba Patera and Syria Planum regions of Mars lose their lithospheric roots in convective overturn events?. *J. Geophys. Res.: Planets*, *108*(E5), 5035. https://doi.org/10.1029/2002JE001492

Shreve, R. L. (1985). Esker characteristics in terms of glacier physics, Katahdin esker system, Maine. *Geol. Soc. Am. Bull.*, *96*(5), 639–646. https://doi.org/10.1130/0016-7606(1985)96<639:ECITOG>2.0.CO;2

Sleep, N. H. (1994). Martian plate tectonics. *J. Geophys. Res.: Planets*, *99*(E3), 5639–5655. https://doi.org/10.1029/94JE00216

Smellie, J. L., Rocchi, S., and Armienti, P. (2011). Late Miocene volcanic sequences in northern Victoria Land, Antarctica: Products of glaciovolcanic eruptions under different thermal regimes. *Bull. Volcanol.*, *73*(1), 1–25. https://doi.org/10.1007/s00445-010-0399-y

Smith, D. E., Zuber, M. T., Solomon, S. C., Phillips, R. J., Head, J. W., Garvin, J. B., Banerdt, W. B., Muhleman, D. O., Pettengill, G. H., ... Duxbury, T. C. (1999). The global topography of Mars and implications for surface evolution. *Science*, *284*(5419), 1495–1503. https://doi.org/10.1126/science.284.5419.1495

Solomon, S. C., and Head, J. W. (1979). Vertical movement in mare basins: Relation to mare emplacement, basin tectonics, and lunar thermal history. *J. Geophys. Res.: Solid Earth*, *84*(B4), 1667–1682. https://doi.org/10.1029/JB084iB04p01667

Solomon, S. C., and Head, J. W. (1980). Lunar mascon basins: Lava filling, tectonics, and evolution of the lithosphere. *Rev. Geophys.*, *18*(1), 107–141. https://doi.org/10.1029/RG018i001p00107

Solomon, S. C., and Head, J. W. (1982). Evolution of the Tharsis province of Mars: The importance of heterogeneous lithospheric thickness and volcanic construction. *J. Geophys. Res.: Solid Earth*, *87*(B12), 9755–9774. https://doi.org/10.1029/JB087iB12p09755

Solomon, S. C., Aharonson, O., Aurnou, J. M., Banerdt, W. B., Carr, M. H., Dombard, A. J., Frey, H. V., Golombek, M. P., Hauck, S. A., … Jakosky, B. M. (2005). New perspectives on ancient Mars. *Science*, *307*(5713), 1214–1220. https://doi.org/10.1126/science.1101812

Stevenson, D. J. (2001). Mars' core and magnetism. *Nature*, *412*(6843), 214–219. https://doi.org/10.1038/35084155

Strom, R. G. (1972). Lunar mare ridges, rings and volcanic ring complexes. In S. K. Runcorn et al. (Eds.), *The Moon* (pp. 187–215). Dordrecht, Netherlands: Springer. https://doi.org/10.1007/978-94-010-2861-5_19

Strom, R. G., Murray, B. C., Belton, M. J. S., Danielson, G. E., Davies, M. E., Gault, D. E., Hapke, B., O'Leary, B., Trask, N., ... Klaasen, K. (1975). Preliminary imaging results from the second Mercury encounter. *J. Geophys. Res.*, *80*(17), 2345–2356. https://doi.org/10.1029/JB080i017p02345

Strom, R. G. (1979). Mercury: A post-Mariner 10 assessment. *Space Sci. Rev.*, *24*, 3–70. https://doi.org/10.1007/BF00221842

Suppe, J. (1983). Geometry and kinematics of fault-bend folding. *Am. J. Sci.*, *283*(7), 684–721. https://doi.org/10.2475/ajs.283.7.684

Tanaka, K. L., Golombek, M. P., and Banerdt, W. B. (1991). Reconciliation of stress and structural histories of the Tharsis region of Mars. *J. Geophys. Res.: Planets*, *96*(E1), 15617–15633. https://doi.org/10.1029/91JE01194

Tanaka, K. L., Skinner, J. A., Jr., Dohm, J. M., Irwin, R. P., III, Kolb, E. J., Fortezzo, C. M., Platz, T., Michael, G. G., and Hare, T. M. (2014). Geologic map of Mars. Reston, VA: U.S. Geological Survey. https://doi.org/10.3133/sim3292

Tjia, H. D. (1970). Lunar wrinkle ridges indicative of strike-slip faulting. *Geol. Soc. Am. Bull.*, *81*(10), 3095–3100. https://doi.org/10.1130/0016-7606(1970)81[3095:LWRIOS]2.0.CO;2

Tornabene, L. L., Osinski, G. R., McEwen, A. S., Wray, J. J., Craig, M. A., Sapers, H. M., and Christensen, P. R. (2013). An impact origin for hydrated silicates on Mars: A synthesis. *J. Geophys. Res.: Planets*, *118*(5), 994–1012. https://doi.org/10.1002/jgre.20082

Walter, T. R., Klügel, A., and Münn, S. (2006). Gravitational spreading and formation of new rift zones on overlapping volcanoes. *Terra Nova*, *18*(1), 26–33. https://doi.org/10.1111/j.1365-3121.2005.00656.x

Ward, A. W., Doyle, K. B., Helm, P. J., Weisman, M. K., and Witbeck, N. E. (1985). Global map of eolian features on Mars. *J. Geophys. Res.: Solid Earth*, *90*(B2), 2038–2056. https://doi.org/10.1029/JB090iB02p02038

Warner, N. H., Golombek, M. P., Sweeney, J., Fergason, R., Kirk, R., and Schwartz, C. (2017). Near surface stratigraphy and regolith production in southwestern Elysium Planitia, Mars: Implications for Hesperian-Amazonian terrains and the InSight lander mission. *Space Sci. Rev.*, *211*(1), 147–190. https://doi.org/10.1007/s11214-017-0352-x

Warren, W. P., and Ashley, G. M. (1994). Origins of the ice-contact stratified ridges (eskers) of Ireland. *J. Sediment. Res.*, *64*(3a), 433–449. https://doi.org/10.1306/D4267DD9-2B26-11D7-8648000102C1865D

Watters, T. R. (1988). Wrinkle ridge assemblages on the terrestrial planets. *J. Geophys. Res.: Solid Earth*, *93*(B9), 10236–10254. https://doi.org/10.1029/JB093iB09p10236

Watters, T. R. (1991). Origin of periodically spaced wrinkle ridges on the Tharsis Plateau of Mars. *J. Geophys. Res.: Planets*, *96*(E1), 15599–15616. https://doi.org/10.1029/91JE01402

Watters, T. R. (1992). System of tectonic features common to Earth, Mars, and Venus. *Geology*, *20*(7), 609–612. https://doi.org/10.1130/0091-7613(1992)020<0609:SOTFCT>2.3.CO;2

Watters, T. R. (1993). Compressional tectonism on Mars. *J. Geophys. Res.: Planets*, *98*(E9), 17049–17060. https://doi.org/10.1029/93JE01138

Watters, T. R., and Robinson, M. S. (1997). Radar and photoclinometric studies of wrinkle ridges on Mars. *J. Geophys. Res.: Planets*, *102*(E5), 10889–10903. https://doi.org/10.1029/97JE00411

Watters, T. R. (2004). Elastic dislocation modeling of wrinkle ridges on Mars. *Icarus*, *171*(2), 284–294. https://doi.org/10.1016/j.icarus.2004.05.024

Watters, T. R., Head, J. W., Solomon, S. C., Robinson, M. S., Chapman, C. R., Denevi, B. W., Fassett, C. I., Murchie, S. L., and Strom, R. G. (2009a). Evolution of the Rembrandt impact basin on Mercury. *Science*, *324*(5927), 618–621. https://doi.org/10.1126/science.1172109

Watters, T. R., Murchie, S. L., Robinson, M. S., Solomon, S. C., Denevi, B. W., André, S. L., and Head, J. W. (2009b). Emplacement and tectonic deformation of smooth plains in the Caloris basin, Mercury. *Earth Planet. Sci. Lett.*, *285*(3–4), 309–319. https://doi.org/10.1016/j.epsl.2009.03.040

Watters, T. R. (2021). A case for limited global contraction of Mercury. *Nat. Commun. Earth Environ.*, *2*(1), 9. https://doi.org/10.1038/S43247-020-00076-5

Watters, T. R. (2022). Lunar wrinkle ridges and the evolution of the nearside lithosphere. *J. Geophys. Res.: Planets*, *127*(3), e2021JE007058. https://doi.org/10.1029/2021JE007058

Weiss, D. K., and Head, J. W. (2014). Ejecta mobility of layered ejecta craters on Mars: Assessing the influence of snow and ice deposits. *Icarus*, *233*, 131–146. https://doi.org/10.1016/j.icarus.2014.01.038

Whitehead, P. W., and Stephenson, P. J. (1998). Lava rise ridges of the Toomba basalt flow, north Queensland, Australia. *Journal of Geophysical Research: Solid Earth*, *103*(B11).

Wilhelms, D. E. (1974). Comparison of Martian and lunar geologic provinces. *J. Geophys. Res.*, *79*(26), 3933–3941. https://doi.org/10.1029/JB079i026p03933

Williams, R. M. E., Irwin, R. P., III, and Zimbelman, J. R. (2009). Evaluation of paleohydrologic models for terrestrial inverted channels: Implications for application to Martian sinuous ridges. *Geomorphology*, *107*(3–4), 300–315. https://doi.org/10.1016/j.geomorph.2008.12.015

Wise, D. U., Golombek, M. P., and McGill, G. E. (1979). Tectonic evolution of Mars. *J. Geophys. Res.: Solid Earth*, *84*(B14), 7934–7939. https://doi.org/10.1029/JB084iB14p07934

Yin, A., and Kelty, T. K. (2000). An elastic wedge model for the development of coeval normal and thrust faulting in the Mauna Loa–Kilauea rift system in Hawaii. *J. Geophys. Res.: Solid Earth*, *105*(B11), 25909–25925. https://doi.org/10.1029/2000JB900247

Yin, A. (2006). Cenozoic tectonic evolution of the Himalayan orogen as constrained by along-strike variation of structural geometry, exhumation history, and foreland sedimentation. *Earth-Sci. Rev.*, *76*(1–2), 1–131. https://doi.org/10.1016/j.earscirev.2005.05.004

Yin, A. (2012a). Structural analysis of the Valles Marineris fault zone: Possible evidence for large-scale strike-slip faulting on Mars. *Lithosphere*, *4*(4), 286–330. https://doi.org/10.1130/L192.1

Yin, A. (2012b). An episodic slab-rollback model for the origin of the Tharsis rise on Mars: Implications for initiation of local plate subduction and final unification of a kinematically linked global plate-tectonic network on Earth.

Lithosphere, *4*(6), 553–593. https://doi.org/10.1130/L195.1

Yin, A., Moon, S., and Day, M. (2021). Landform evolution of Oudemans crater and its bounding plateau plains on Mars: Geomorphological constraints on the Tharsis ice-cap hypothesis. *Icarus*, *360*, 114332. https://doi.org/10.1016/j.icarus.2021.114332

Yue, Z., Li, W., Di, K., Liu, Z., and Liu, J. (2015). Global mapping and analysis of lunar wrinkle ridges. *J. Geophys. Res.*: *Planets*, *120*(5), 978–994. https://doi.org/10.1002/2014JE004777

Yue, Z., Michael, G. G., Di, K., and Liu, J. (2017). Global survey of lunar wrinkle ridge formation times. *Earth Planet. Sci. Lett.*, *477*, 14–20. https://doi.org/10.1016/j.epsl.2017.07.048

Zaki, A. S., Pain, C. F., Edgett, K. S., and Giegengack, R. (2018). Inverted stream channels in the Western Desert of Egypt: Synergistic remote, field observations and laboratory analysis on Earth with applications to Mars. *Icarus*, *309*, 105–124. https://doi.org/10.1016/j.icarus.2018.03.001

Zhao, J., Huang, J., Kraft, M. D., Xiao, L., and Jiang, Y. (2107). Ridge-like lava tube systems in southeast Tharsis, Mars. *Geomorphology*, *295*, 831–839.

Zhong, S. J. (2009). Migration of Tharsis volcanism on Mars caused by differential rotation of the lithosphere. *Nat. Geosci.*, *2*(1), 19–23. https://doi.org/10.1038/ngeo392

Zuber, M. T., and Aist, L. L. (1990). The shallow structure of the Martian lithosphere in the vicinity of the ridged plains. *J. Geophys. Res.*: *Solid Earth*, *95*(B9), 14215–14230. https://doi.org/10.1029/JB095iB09p14215

Zuber, M. T. (1995). Wrinkle ridges, reverse faulting, and the depth penetration of lithospheric strain in Lunae Planum, Mars. *Icarus*, *114*(1), 80–92. https://doi.org/10.1006/icar.1995.1045

Zuber, M. T. (2001). The crust and mantle of Mars. *Nature*, *412*(6843), 220–227. https://doi.org/10.1038/35084163